Structural Transitions of Myosin Associated with Force Generation in Spin-labeled Muscle Fibers

A DISSERTATION
SUBMITTED TO THE FACULTY OF THE GRADUATE SCHOOL
OF THE UNIVERSITY OF MINNESOTA
BY

Ryan Nicholas Mello

IN PARTIAL FULFILLMENT OF THE REQUIREMENTS
FOR THE DEGREE OF
DOCTOR OF PHILOSOPHY

David D. Thomas, advisor

June 2012

Acknowledgements

There are many people who have provided me with support in one way or another as I completed my PhD. To all of you, I am deeply thankful.

First, I want to acknowledge my advisor **Dr. David Thomas**. Without his support, guidance and encouragement this work would not have been possible. Dr. Thomas is a gifted scientist and leader, and from him I have learned a great deal about science and life. Dr. Thomas is a living example of “do what you love, and love what you do.”

I also want to thank my committee members: **Dr. Dawn Lowe**, **Dr. Vincent Barnett** and **Dr. Russell Ritenour**. They have provided invaluable instruction in my graduate courses an guidance as I progressed through graduate school.

Octavian Cornea and **Sarah Blakely**, I am not sure what I would have done without you two. Over the past six years the two of you have had the answer to literally every question I have asked of you. Your expertise has saved me countless hours. Thank you for your knowledge and friendship.

I want to extend a special thanks to the senior graduate students, now postdoctoral fellows, who taught me the practical aspects of being a biophysicist and a graduate student: **Dr. David Kast**, **Dr. Andrew Thompson** and **Dr. Roman Agafonov**. Outside the lab, Dave Kast was always primed to have fun, Andrew’s wit was always entertaining and Roman’s constant question “Why?” always kept me on my toes.

Over the past six years I have been fortunate to have outstanding technical support in areas where my knowledge was lacking. **Florentin Nitu**, **Leanne Kolb** (now Anderson), **Eunice Song**, **Christina Yi**, **Evan Smith, Edmund Howard** and **Tyler**

Miller, I am grateful for your assistance. I have also had the opportunity to work with some talented and motivated undergraduates, **Bobby Harris** and **Doug Deitchler**.

Thank you **Jesse McCaffrey** and **Zach James** for insightful conversations about EPR spectroscopy. Thanks **John Rubin** and **Yun Lin** for helping my pursuit of a career in medicine; maybe we will work together in the clinic someday. And thank you **Becca Moen**, **Ben Binder**, **Karl Petersen** and **Dr. Bengt Svensson** for all the help with the BSL project.

I also need to thank my in-laws. **Rick** and **Jean Bearden** have shown me unconditional love and support and provided countless meals. Thank you **Camille Bearden** for all the fun times you have spent with me and Caili, and your priceless Kristen Wiig impressions. Thanks **Alex Bearden** for making me laugh uncontrollably, and thank you **Meredith Bearden** for being quite possibly the sweetest person on earth. And **Patty Bearden**, thanks for keeping life interesting with your attitude. You are all very important in my life.

And finally, I need to thank my extended family for providing love, support, and fun over the past 28 years. **Grandpa** and **Grandma Skatrud**, you have shaped my life since the moment I was born and still touch my life to this day. **Grandpa** and **Grandma Mello**, you are missed greatly and your love will always be with me. **David Skatrud**, **John Skatrud**, **Kari** and **Matt McCreedy** and **John** and **Cheri Mello,** I can't thank you enough for all the joy you have brought into my life (Duke basketball games, skiing, ping-pong, inspiration, beer…the list goes on). **Caili**, **Danielle**, **Frank** and **Mary**, this is for you (next page).

Dedication

To my wife, ***Caili Mello***
"If I know what love is, it is because of you" ~ Hermann Hesse

And

To my parents and sister, ***Frank, Mary and Danielle Mello***
"Be brave. Take risks. Nothing can substitute experience." ~ Paulo Coelho

Abstract

Muscle contraction is driven by the actin-activated hydrolysis of ATP by myosin, resulting in the relative sliding of actin and myosin filaments. Current models propose that filament sliding is driven by a structural transition of myosin's catalytic domain (CD) and light chain domain (LCD). The goal of this research is to measure structural transitions of myosin II (muscle and nonmuscle) that are associated for force generation. Structural measurements were made using electron paramagnetic resonance (EPR) spectroscopy. This work is comprised of two separate, but related, projects.

In the first project (Chapter 3), thiol crosslinking and EPR were used to resolve structural transitions of myosin's LCD and CD that are associated with force generation. Spin labels were incorporated into the LCD of muscle fibers by exchanging spin-labeled regulatory light chain (RLC) for endogenous RLC, with full retention of function. LCD orientation and dynamics were measured in three biochemical states: relaxation (A.M.T), post-hydrolysis intermediate (A.M′.D.P), and rigor (A.M.D). To trap myosin in a structural state analogous to the elusive post-hydrolysis ternary complex A.M′.D.P, we used pPDM to crosslink SH1 (Cys707) to SH2 (Cys697) on the CD. EPR showed that the LCD of crosslinked fibers has an orientational distribution intermediate between relaxation and rigor, and saturation transfer EPR revealed slow rotational dynamics indistinguishable from that of rigor. Similar results were obtained for the CD using a bifunctional spin label to crosslink SH1 to SH2, but the CD was more disordered than the LCD. We conclude that SH1-SH2 crosslinking traps a state in which both the LCD and CD are in a structural state intermediate between relaxation (highly disordered and

microsecond dynamics) and rigor (highly ordered and rigid), supporting the hypothesis that the crosslinked state is an A.M′.D.P analog on the force generation pathway.

In the second project, we present a method for obtaining high-resolution structural information of proteins using EPR of a bifunctional spin label (BSL). Two complimentary EPR techniques were employed to measure dynamics and orientation (conventional EPR) and intraprotein distances (dipolar electron-electron resonance). The exploitation of BSL is a key feature of this work. BSL attaches at residue positions *i* and *i*+4, which drastically restricts probe motion compared to monofunctional probes. For comparison, measurements were also made with the monofunctional spin label MSL. Subfragment 1 of *Dictyostelium* myosin II (S1dC) was used to exemplify the increased resolution provided by BSL. Using this approach, we demonstrate with experiments that BSL significantly increases resolution when measuring distance and orientation compared to MSL. And while this work does focus on the methodology, there is significant biological insight into myosin's nucleotide-dependent structural transitions.

Table of Contents

List of Tables

List of Figures

Abbreviations

A, actin

ADP or D, adenosine diphosphate

ATP or T, adenosine triphosphate

BSL, 3,4-bis-(methanethiosulfonyl-methyl)-2,2,5,5-tetramethyl-2,5-dihydro-1h-pyrrol-1-yloxy

CD, myosin catalytic domain

Cys, cysteine

LCD, myosin light chain domain

M, myosin

MSL, N-(1-oxy-2,2,6,6-tetramethyl-4-piperidinyl)maleimide.

P or P_i , inorganic phosphate

pPDM, N,N′-(1,4-phenylene)dimaleimide

S1dC, subfragment 1 of *Dictyostelium discoideum* myosin II

Tn, troponin

Chapter 1: Introduction to Muscle Contraction & Myosin

Many processes that are essential to the existence of living organisms require self-propelled movement. Examples include chromosome separation during cell division, molecular transport within cells, the beating action of a heart and the inhalation of fresh air into lungs. The powerhouses for these forms of movement, and many others, are a group of biological macromolecules known as motor proteins. Motor proteins use energy derived from ATP hydrolysis to do mechanical work. There are three types of motor proteins: kinesin, dynein and myosin. This work is focused on myosin, specifically myosin II (which includes muscle myosin).

1.1 Skeletal Muscle Contraction

Muscle contraction is an intricate process requiring precise coordination of neurotransmitters, ions, nucleotides, and proteins. To investigate skeletal muscle contraction on a molecular level, it is important to first examine muscle structure from a macroscopic to microscopic scale (**Figure 1**). Moving from the gross visualization of muscle tissue, the first subunit is the fascicle which is composed of a parallel bundle of muscle cells (also referred to as muscle fibers). Each muscle fiber contains several myofibrils, and each myofibril is made of several sarcomeres. The sarcomere is the organelle within the muscle cell that is responsible for movement (1). Each sarcomere contains an interdigitating lattice of myosin and actin filaments, known as the thick (myosin) and thin (actin) filaments. Muscle contraction is driven by the actin-activated

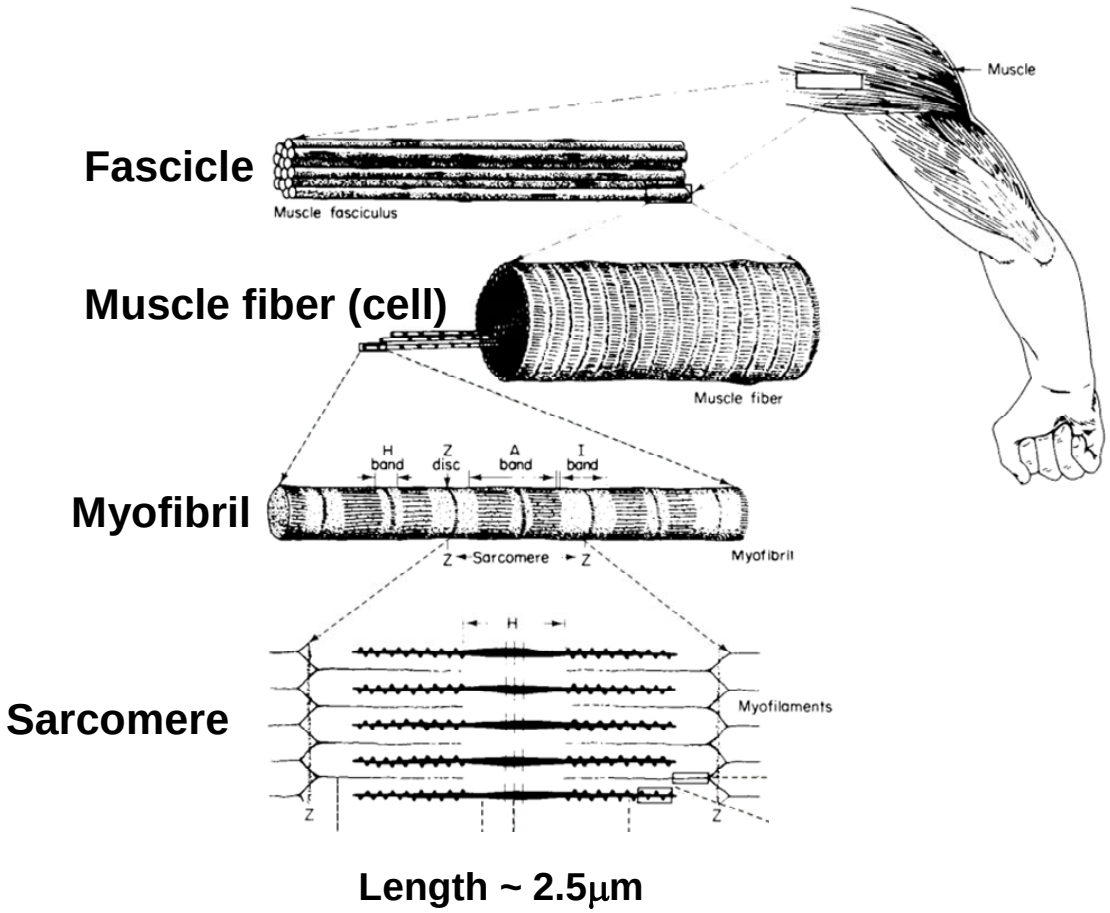

Figure 1 Skeletal muscle structure.
Adapted from Bloom and Fawcett, *Textbook of Histology*, 11th ed. Philadelphia, WB Saunders, 1986 page 282.

hydrolysis of ATP by myosin, resulting in the relative sliding of actin and myosin filaments (**Figure 2**).

Myosin is the molecular motor driving muscle contraction, however, force production involves several other contractile proteins. As mentioned above, the primary component of the thin filament is actin. Actin is a 43kD protein that myosin binds during muscle contraction. Under physiological conditions, actin polymerizes to form an α-helical double-stranded filament. The proteins troponin and tropomyosin bind to the actin filament backbone, and aid in the Ca^{2+} regulation of skeletal muscle contraction.

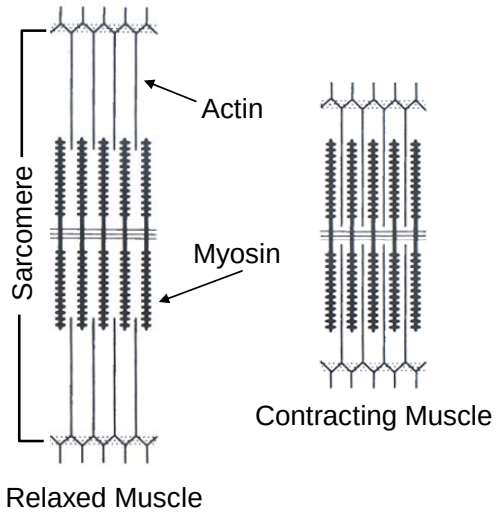

Figure 2 The contracting sarcomere.
Schematic representation of the fundamental unit of muscle contraction, the sarcomere, emphasizing the relative sliding of actin and myosin filaments during contraction. The sarcomere is composed of interdigitating myosin (thick) and actin (thin) filaments. Adapted from (1).

Tropomyosin is a 65 kDa protein that forms an α-helical dimer and binds to the actin filament. Troponin (Tn) is a three subunit complex consisting of TnC (18 kDa), TnT (30 kDa) and TnI (30 kDa). The Tn complex binds Ca^{2+} and controls the conformation of tropomyosin on actin. During relaxation, cytosolic Ca^{2+} is low (~ 0.1 μM), and tropomyosin is locked over the myosin biding site on actin. During contraction, the sarcoplasmic reticulum releases Ca^{2+}, increasing the cytoplasmic Ca^{2+} to ~ 10 μM. TnC then binds Ca^{2+} and undergoes a conformational change. This conformational change is relayed to TnT and TnI. TnI then unlocks tropomyosin from the myosin binding site, enabling myosin to bind actin.

In addition to those mentioned above, there are other proteins associated with the thick (myosin) and thin (actin) filaments. Titin is a massive protein (MW greater than 3 MDa) that contributes to muscle assembly, resting tension and sarcomere length (2). Myosin-Binding protein-C (c-protein) contributes to the formation and stabilization of

thick filaments and is thought to modulate contractility by interacting with both thick and thin filaments (3). Nebulin is associated with the thin filament, and is thought to play a role in the regulation of thin filament length and muscle contractility (4). There are additional proteins within the sarcomere, but the ones mentioned above are those predominantly associated with the thick and thin filaments.

Muscle contraction is produced by the actin-activated hydrolysis of ATP by myosin (5). This results in the relative sliding of actin and myosin filaments (**Figure 2**). Mechanistic models propose that filament sliding is driven by a structural transition of the myosin catalytic domain (CD) from a dynamically disordered state of weak actin binding to an ordered state of strong actin binding, and a lever arm rotation of the light-chain domain (LCD)(6-9). This work presented herein focuses on these force-generating structural transitions of myosin.

1.2 Myosin Structure

Myosin is a dimeric protein with a molecular weight of approximately 500kD. Each protomer contains a 120 kDa head and a long α-helical C-terminal tail. The two tails bind to form a coiled coil, which unites the two heads (**Figure 3**, top). The myosin head (which can be isolated proteolytically as subfragment 1, or S1) consists of the N-terminal catalytic domain (CD) and the light-chain domain (LCD) (**Figure 3**, bottom). The CD contains the ATP-binding pocket and the actin-binding region. The LCD contains a single α-helix, extending C-terminally from the CD, to which are bound two light chains, the essential light chain (ECL) and the regulatory light chain (RLC).

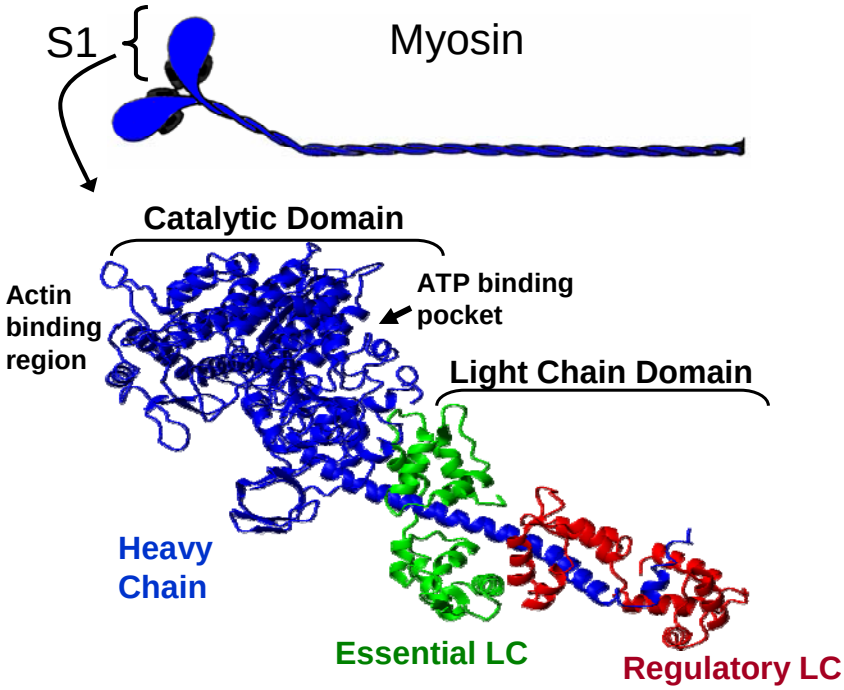

Figure 3 Myosin Structure.
Top: Cartoon illustrating the dimeric myosin molecule including the long α-helical tale and two heads. Bottom: Crystal structure of the myosin head (S1) (10). The catalytic domain contains the actin binding region and the ATP binding pocket. The two light chains are shown in green (essential light chain) and red (regulatory light chain).

1.3 The Actomyosin ATPase Cycle

During ATPase cycling, the interaction between myosin and actin can be classified (to a first approximation) as either weak, when ATP is bound to myosin, or strong, when ADP or no nucleotide is bound (11). Mechanistic models propose that force generation in muscle is driven by a structural transition of the myosin catalytic domain (CD) from a dynamically disordered state of weak actin binding to an ordered state of strong actin binding, and a lever arm rotation of the light-chain domain (LCD)(6-10).

A schematic model demonstrating the actomyosin ATPase is shown in **Figure 4**. This model (adapted from (12)) focuses on the coupling between myosin's force-producing structural transitions (based on crystal structures (13,14) and spectroscopy (11)) and biochemical state (defined by the active site ligand) and actin binding properties of myosin. The post-powerstroke rigor state (**Figure 4**, A) is populated when myosin is in apo or ADP biochemical states. In rigor myosin has a strong actin affinity (K_d < 1 μM) and the CD is well oriented on actin with slow (ms) dynamics. After ADP release, ATP binding (**Figure 4**, B) weakens the actin-myosin interaction, dissociating actin from myosin (relaxation). In relaxation myosin has a weak affinity for actin (K_d =

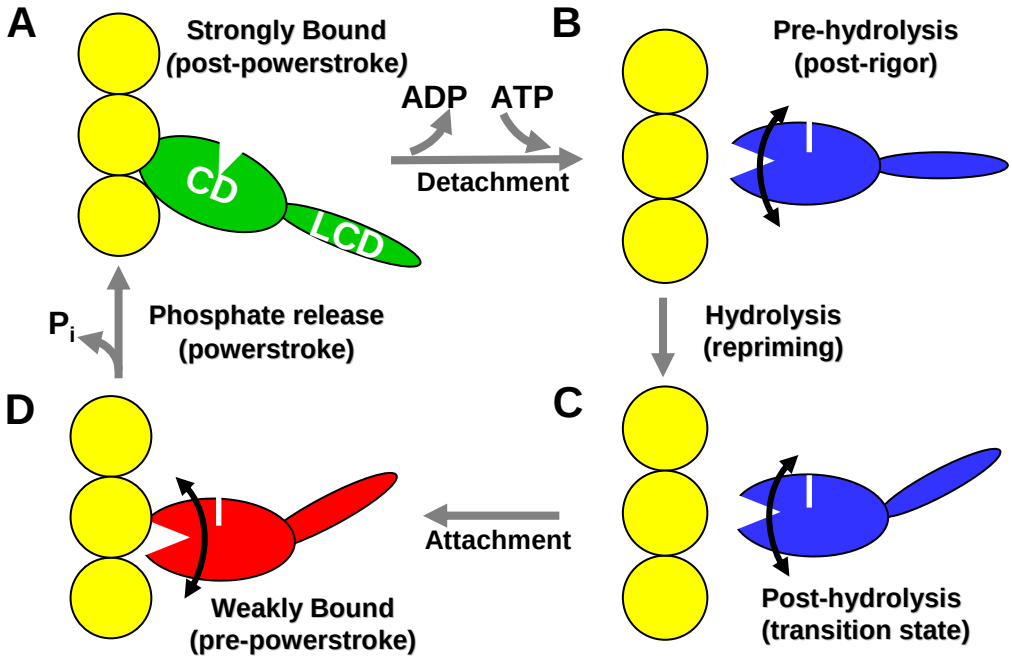

Figure 4 The actomyosin ATPase cycle.
Proposed structural changes of myosin S1 during ATPase cycling. This model focuses on the coupling between the force-producing structural changes and myosin's biochemical state (defined by the active site ligand) and actin binding properties. Adapted from (12).

100 μM) and the CD is dynamically disordered (μs dynamics). Myosin then hydrolyzes ATP to ADP.P_i, and undergoes a repriming (**Figure 4**, B-C). Next, the post-hydrolysis complex forms a weak binding complex with actin (**Figure 4**, C-D) (5), and there is evidence that force generation begins in this biochemical state, before phosphate is released but after isomerization (**Figure 4**, C-D) (15,16). The powerstroke is then completed as P_i is released, and myosin undergoes a force producing weak-to-strong transition (also referred to as a disorder-to-order transition) (**Figure 4**, D-A).

1.4 Motivation for Research

For several reasons, the structure of muscle (particularly striated muscle) has made the muscle fiber an attractive system for investigating movement in living organisms (12). First, the primary proteins involved in muscle contraction, actin and myosin, comprise 80% of the structural proteins present within the cell, enabling the isolation of relatively large amounts of these proteins for characterization. Second, the contractile organelle, the sarcomere, is highly organized and repetitive. Such organization has made it possible to deduce structural information, on the molecular level, from x-ray diffraction and microscopy. Third, muscle contraction is macroscopic. Unidirectional shortening of muscle has made it possible to characterize the mechanical properties of muscle such as length, force and velocity. The results, models and theories discussed in sections 1.1 – 1.3 represents a small subset of the research done to understand muscle contraction on a molecular level. Several disciplines, including biochemistry, physiology, microscopy, crystallography, and spectroscopy, have contributed to the understanding of

muscle contraction on the molecular level. These techniques and theories have also been applied to the study of the other molecular motors, kinesin and dynein.

In this work, we used electron paramagnetic resonance spectroscopy (EPR) to investigate muscle contraction on a molecular level. EPR is an ideal tool for studying a dynamic process such as muscle contraction because it is sensitive to both orientation and dynamics (sections 2.6 and 2.7). Measurements using spin-labeled myosin (a spin label is a small organic molecule with a stable unpaired electron) were made with myosin bound to actin in oriented muscle fiber bundles. Therefore, unlike solution work where myosin is tumbling isotropically, we were able to orientate myosin using the intrinsic order of the muscle fiber. Fiber bundles were oriented with the long axis parallel or perpendicular to the applied magnetic field (H), making it possible to measure changes in myosin orientation relative to the actin filament axis. Spectra were acquired while perfusing the fiber bundle with solution, making it possible to change the biochemical state of the muscle during acquisition. Chapter 3 and 4 summarize this work, and demonstrate the power of this approach for making high resolution structural measurements of myosin in the presence of actin. Structural measurements were made in several biochemical states, but special emphasis was placed on myosin's structural transitions that initiate force generation (**Figure 4**, D-A). These post-hydrolysis early-force complexes have remained elusive and difficult to study because actin (i) greatly accelerates the rate of P_i release, and (ii) shifts the equilibrium constant for hydrolysis toward the prehydrolysis state by a factor of 20 (17).

Chapter 2: Electron Paramagnetic Resonance

Electron Paramagnetic resonance is a technique capable of detecting unpaired electrons. When an unpaired electron is placed in strong magnetic field, incident microwaves may be absorbed causing electron-spin reorientation (18). The EPR spectrum can then be used to characterize the g-factor for the sample.

$$g = \frac{h\nu}{\beta H_0}$$

The g-factor is a measure of the local magnetic field experienced by the electron, and it is a characteristic quantity of electron environment. Additionally, the observed g-factor is often anisotropic, that is, its value is dependent on the orientation of the molecule in the magnetic field (18). Consequently, EPR is useful for not only detecting unpaired electrons, but for gaining insight about the electron's environment, orientation, and dynamics. In this work, EPR was used to measure myosin orientation and dynamics. The remainder of Chapter 2 covers the basic principles of EPR spectroscopy, and its application to measuring myosin orientation and dynamics.

2.1 Angular Momentum and Spin

In classical mechanics, a rigid body possesses two kinds of angular momentum; (a) orbital angular momentum (**L** = **r** x **p, r** is the position vector relative or origin and **p** is the momentum) associated with the motion of the center of mass and (b) spin angular momentum (**S** = ***I*****ω**, ***I*** is the moment of inertia and **ω** is angular velocity) associated with

motion about the center of mass (19). Similar to the earth revolving around the sun and rotating about its axis, electrons posses orbital and spin angular momentum. For electrons, the orbital angular momentum is associated with motion around the atomic nucleus. However, the spin angular momentum of an electron has nothing to do with its motion in space, even though the spin angular momentum of an electron is often compared to the classical notion of spin. This comparison is a useful tool conceptually, but it fails to describe reality because electrons are believed to be structureless point particles (19). Considering this ambiguous nature of electrons, it is reasonable to say that electrons have an intrinsic spin angular momentum (**S**), though not in a classical sense, in edition to their extrinsic orbital angular momentum (**L**). The spin angular momentum **S** can be described by the spin quantum number m_s, where $m_s = \pm ½$. Just as nuclear magnetic resonance spectroscopy and magnetic resonance imaging manipulate spin states of protons and neutrons, electron paramagnetic resonance manipulates the spin states of electrons.

2.2 The Zeeman Effect

Magnetic resonance refers to the absorption of a photon causing spin to reorient, or flip. In EPR it is the electron spin that flips after absorbing a photon, but only in the presence of a strong magnetic field. In the presence of a magnetic field, the degeneracy of the spin states is broken. That is, in the absence of a magnetic field , ΔE between spin states is 0. In the presence of a magnetic field **H**, ΔE is nonzero. This phenomenon is known as the Zeeman Effect (**Figure 5**), and is explained below.

The magnetic moment of an electron is

$$\boldsymbol{\mu} = \gamma \mathbf{S}$$

where γ is the gyromagnetic ratio (-1.76 x 10^7 rad/(s*G) for an electron) and **S** is the spin angular momentum. The energy of a magnetic moment is a function of the magnetic moment $\boldsymbol{\mu}$ and the magnetic field **H**. If the magnetic field is oriented along the z-axis, the energy can be expressed as

$$E = -\boldsymbol{\mu} \bullet \mathbf{H} = -\gamma \mathbf{S} \bullet \mathbf{H} = -\gamma S_z \bullet H$$

S_z can only have values of $m_s\hbar$, so

$$E = -\gamma m_s \hbar H$$

The gyromagnetic ratio γ is expressed as $-g\beta/\hbar$, therefore

$$E = m_s g \beta H$$

Now, in the presence of an applied magnetic field, there are two energy levels

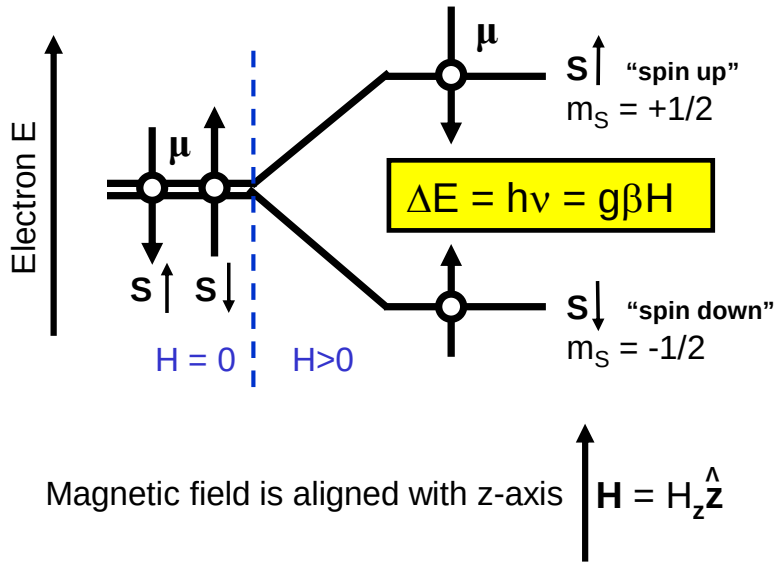

Figure 5 The Zeeman Effect.
Electron energy level splitting in a magnetic field due to the Zeeman Effect. Magnetic resonance occurs when electromagnetic radiation of the appropriate energy is applied perpendicular to the external magnetic field H. Adapted from (18).

corresponding to the two spin states:

$$m_s = + ½ \text{ “spin up”: } E = (½)g\beta H$$

$$m_s = - ½ \text{ “spin down”: } E = (-½)g\beta H$$

Therefore, the energy difference between the two spin states is

$$\Delta E = E_{up} - E_{down} = g\beta H$$

In EPR spectroscopy, magnetic resonance occurs when the microwave energy ($h\nu$) equals ΔE (eq. 2.1, **Figure 5**), which is referred to as the resonance condition

$$h\nu = g\beta H \qquad \textbf{[eq. 2.1]}$$

2.3 The EPR spectrometer

A schematic showing the basic components of an EPR spectrometer is shown in **Figure 6**. In it simplest form, an EPR spectrometer consists of a magnet, a photon (microwave) source, and a resonant cavity. The magnetic field is supplied by an electromagnet. For X-band EPR (used in this work), the microwave frequency is ~ 9.5 GHz, and is supplied by a Gunn Diode. The resonator, where the sample is placed, is called a cavity. The resonance condition (eq. 2.1) can be met by sweeping the magnetic field or the microwave frequency. It is simpler, from an engineering standpoint, to vary the magnetic field strength by varying the current through the electromagnet. Therefore, in EPR spectroscopy the magnetic field is swept while the microwave frequency is held constant. Detection of the absorption signal is improved by modulating the magnetic field,

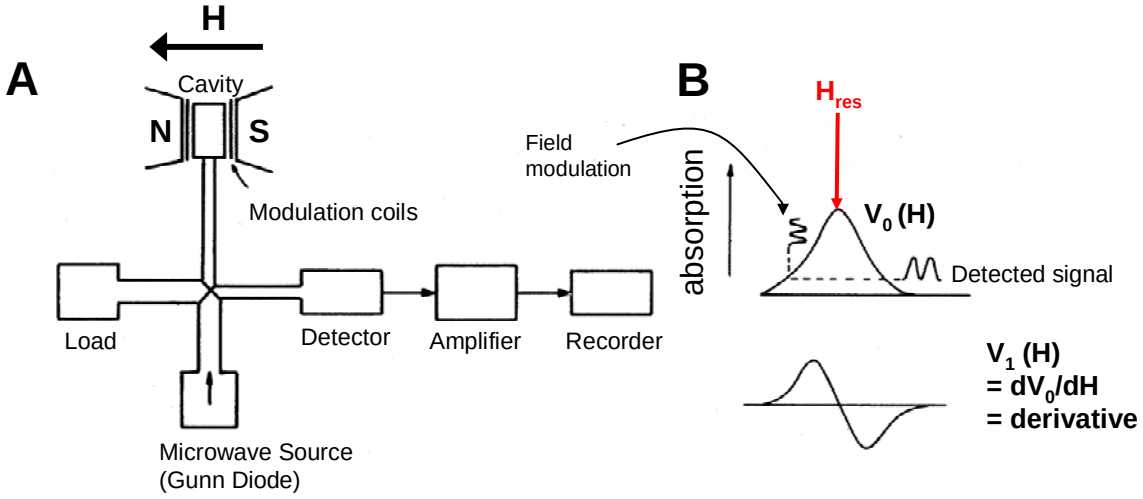

Figure 6 The basics of an EPR spectrometer.
A: Simple schematic highlighting the essential components of an EPR spectrometer. B: EPR spectrum obtained by field modulation and phase-sensitive detection ate the modulation frequency. Adapted from (18).

generally a 100 kHz sinusoidal modulation (18). If this modulation amplitude is less than the linewidth of the absorption signal, and the detector is sensitive to the phase of the signal, the detected signal appears as a derivative of the absorption spectrum (18) (**Figure 6**, B). That is, EPR spectra are viewed as the derivative of absorption (V_1) vs. magnetic field strength (H), rather than absorption (V_0) vs. H.

2.4 Site-Directed Spin Labeling

As explained above, EPR spectroscopy detects unpaired electrons. In biological systems, unpaired electrons occur in some transition metal ions and in free radicals. Free radicals are usually highly reactive and therefore unstable. In order to make structural measurements on myosin, we have used site-directed spin labeling (SDSL). A spin label is a small organic molecule with a stable unpaired electron and the ability to bind to a specific site on another molecule. The unpaired electron is usually on the nitrogen atom in an N-O

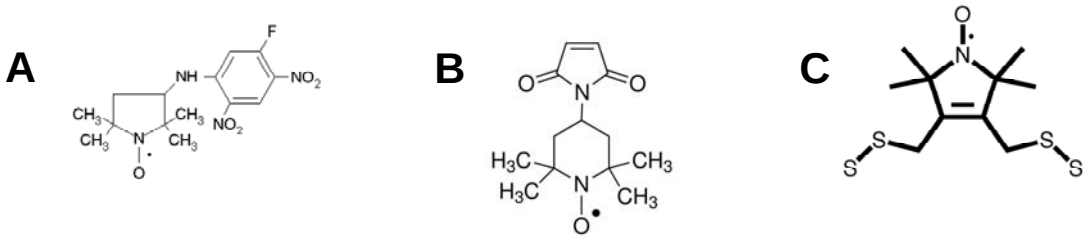

Figure 7 Nitroxide spin labels.
A: 3-(5-f luoro-2,4-dinitroanilino)-2,2,5,5-tetramethyl-1-pyrrolidinyloxy, abbreviated as FDNASL. B: 4-maleimido-2,2,6,6-tetramethyl-1-piperidinyloxy or 4-Maleimido-TEMPO, abbreviated as MSL. C: Trans-3,4-bis-(methanethiosulfonylmethyl)-2,2,5,5-tetramethylpyrrolidin-1-yloxy Radical, abbreviated as BSL.

(nitroxide) bond, hence the name nitroxide spin label. The nitroxide spin labels used in this work (**Figure 7**) bind selectively to the amino acid cysteine (Cys). Given this selectivity, it is possible to attach a spin label to a specific area of interest. Muscle fibers contain several cysteine residues, however strategic labeling conditions makes it possible to selectively label SH1 (Cys707) and/or SH2 (Cys697) on the myosin CD (5). Alternatively, protein engineering can be used to mutate out all reactive Cys residues, and then introduce a labeling site (Cys residue) at resides other than SH1 and SH2 (20,21). In this work, both techniques were used to obtain selective spin-labeling in myosin.

2.5 Nuclear Hyperfine Interaction

With the use of nitroxide spin labels, the hyperfine interaction becomes relevant. The hyperfine interaction is due to the magnetic interaction between the dipole moments of the electron and nearby nuclei. In the case of a nitroxide spin label, it is the magnetic moment of the nitrogen nucleus. Due to the hyperfine interaction, each electron spin state is split into (2I + 1) energy states, where I = nuclear spin. For nitrogen, I = 1, yielding three additional energy states for each electron spin state.

From section 2.2, which describes the Zeeman Effect, the Hamiltonian for an unpaired electron in a magnetic field, neglecting the hyperfine interaction, can be written as

$$\mathcal{H}_{zeeman} = g\beta HS_z/\hbar$$

The hyperfine interaction adds an additional term to the Hamiltonian.

$$\mathcal{H} = \mathcal{H}_{zeeman} + \mathcal{H}_{hyperfine} = g\beta HS_z/\hbar + hA(I_z/\hbar)(S_z/h)$$

Where A is the energy of the hyperfine interaction, I_z is the spin of the nucleus. Considering the Zeeman interaction and hyperfine splitting, the energy of the electron is

$$E = g\beta H m_s + hAm_I m_s$$

Selection rules determining the "allowed" electron energy-level transitions state that the change in electron spin $m_s = \pm ½$, and the change in nuclear spin $m_I = 0$. Thus, there are three possible transitions (**Figure 8**, A), and the difference in energy is

$$\Delta E = g\beta H + hAm_I \qquad \textbf{[eq. 2.2]}$$

These three transitions lead to the three-lined EPR spectrum of a nitroxide spin label (**Figure 8**, B), with a splitting T between lines, where $T = hA/g\beta$. Substituting T into eq. 2.2, and solving for H (or H_{res}, when $\Delta E = h\nu$) yields

$$H_{res} = h\nu/g\beta - m_I T \qquad \textbf{[eq. 2.3]}$$

The following sections will examine the anisotropic nature of g and T.

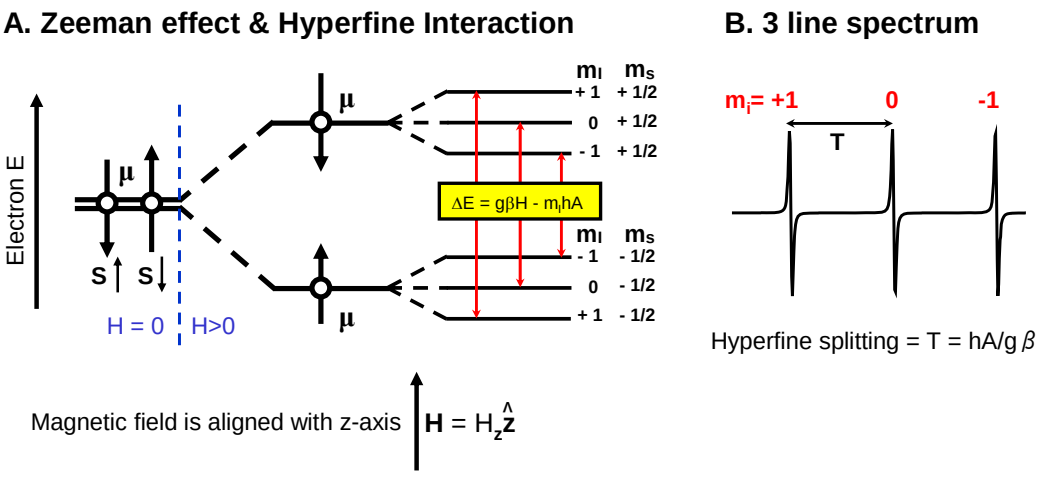

Figure 8 The Hyperfine Interaction.
A: For nitroxide spin labels, energy level splitting from the Zeeman effect and nuclear hyperfine interaction leads to three transitions between electron spin states. B: Three lined spectrum characteristic of nitroxide spin labels.

2.6 EPR is Sensitive to Orientation

In this work, EPR is used to determine the orientation of a spin label's principal axes with respect to an oriented assembly (the actin filament). The first step in this effort is spin-labeling myosin. Strategically labeling myosin has made it possible to achieve rigid coupling between the spin label and peptide backbone. Therefore, we can make the assumption that the behavior of the spin label is characteristic of the peptide backbone. The orientational sensitivity of EPR arises from the anisotropic interaction of the nitroxide group on the spin label with the applied magnetic field **H**. This section examines the effect of orientation on the position and shape of lines in an EPR spectrum.

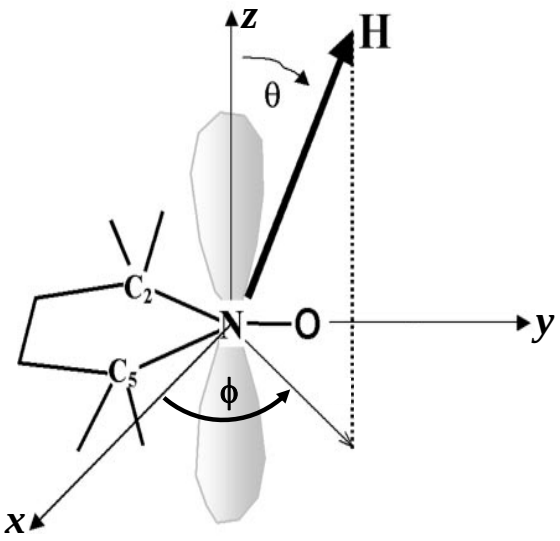

Figure 9 Orientation of the applied magnetic field in the spin label coordinate frame.
The coordinate frame of the spin label is such that the x-axis is aligned with the N-O bond and the z-axis is perpendicular to the aromatic ring (approximately parallel with the unpaired electron's π-orbital). The vector representing the applied field **H** is defined by θ and ϕ. Adapted from (22).

Recall from eq. 2.3 that the resonant condition is dependent on g and T.

$$H_{res} = h\nu/g\beta - m_I T$$

Due to the asymmetry in the electron density of the π-orbital of the unpaired electron in the nitroxide bond (**Figure 9**), both g and T are dependent on orientation of the nitroxide group relative to the applied magnetic field H. If the spin label (probe) coordinate frame is defined as shown in **Figure 9**, the orientation of the magnetic field in the probe's frame is defined by θ and ϕ. Using this probe frame, g (unitless) and T (Gauss) are given by

$$g(\theta,\phi) = g_x\sin^2\theta\cos^2\phi + g_y\sin^2\theta\sin^2\phi + g_z\cos^2\theta$$

$$T(\theta,\phi) = (T_x^2\sin^2\theta\cos^2\phi + T_y^2\sin^2\theta\sin^2\phi + T_z^2\cos^2\theta)^{1/2}$$

And the resonant condition now becomes

$$H_{res} = h\nu/g(\theta,\phi)\beta - m_I T(\theta,\phi) \quad \textbf{[eq. 2.4]}$$

From eq. 2.4 it is evident that the spin label's orientation affects the position of the center of the spectrum ($h\nu/g(\theta,\phi)\beta$) and the splitting between the lines $T(\theta,\phi)$. **Figure 10** illustrates the orientational sensitivity of EPR when the magnetic field is along the x-, y- and z-axis of the spin labels coordinate frame.

The spectra in **Figure 10** are representative of three different discrete orientations, and they emphasize that EPR is highly sensitive to the

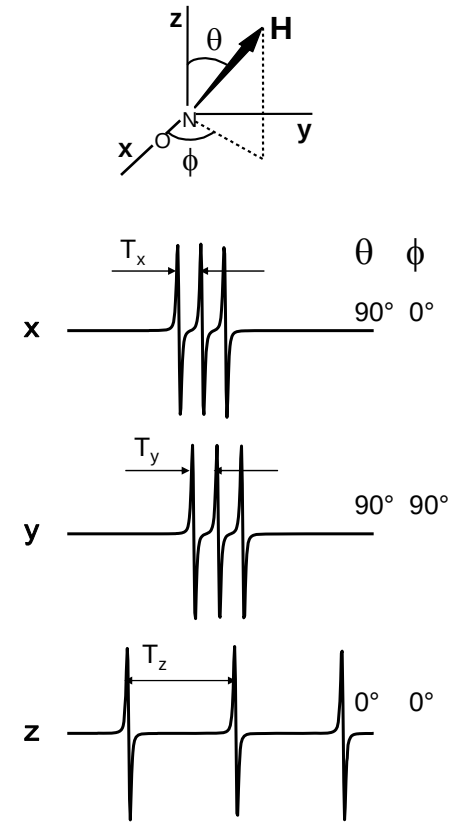

Figure 10 Sensitivity of EPR to orientation.

orientation of the nitroxide group relative to the applied field H. Another important feature of EPR is its sensitivity to orientational distributions, or the amount of disorder present in a system (**Figure 21)**. This is particularly useful for investigating biological systems because changes in disorder are prevalent and relate directly to function (11).

It is evident from **Figure 21** that EPR spectra change with disorder. That is, as the width of the distribution increases ($\Delta\theta'$ increases) the lines in the EPR spectrum broaden. These changes arise from the dependence of T and g on θ and ϕ. However, at X-band it is common to assume axial symmetry ($T_x = T_y$ in **Figure 10**), meaning that the spectra are insensitive to ϕ. This assumption is acceptable at X-band (9.5 GHz), but not at higher frequencies. In this work, we assume a Gaussian distribution to model the disorder of the system, meaning there is a Gaussian distribution of θ. As a result, the spectrum representing a system with some amount of disorder is a superposition of numerous composite spectra with different centers and splitting. Simulations showing this result are shown in **Figure 21**. In this discussion, and the simulations shown in **Figure 21**, the assumption is made that the spin label is immobilized on the nanosecond timescale.

2.7 EPR is sensitive to Dynamics

In this work, two types of EPR experiments are used for measuring dynamics: (i) Conventional EPR and (ii) Saturation Transfer EPR (STEPR). Conventional EPR is sensitive to rotational motion with $\tau_R \sim 10^{-11} - 10^{-6}$ s, and STEPR is sensitive to $\tau_R \sim 10^{-7} - 10^{-3}$ s, where τ_R is the rotational correlation time. In all other sections, the term EPR is

used to refer to conventional EPR and STEPR will be referred to explicitly. This section will cover the basics of both techniques.

2.7.1 Conventional EPR

When setting up an EPR experiment, the parameters for conventional EPR and STEPR are different. Some of these differences are evident in the nomenclature used to describe conventional EPR and STEPR spectra. The conventional EPR spectrum is often referred to as V_1. The V refers to the absorption mode, with the alternative being dispersion mode, U. In this work, conventional EPR and STEPR are acquired in absorption mode. The numerical subscript "1" refers to the modulation harmonic. Conventional EPR spectra are acquired using 100 KHz modulation frequency ν_m, which is the first harmonic. It is also important to note that in this work conventional EPR spectra are acquired at a non-saturating microwave power (this is not the case for STEPR).

Conventional EPR is sensitive to rotational motions with τ_R comparable to or faster than the spin-spin relaxation time T_2 (~ 10^{-8} s). In this time range, the motion of the label partially or completely averages out the g and T anisotropy observed in **Figure 10** and **Figure 21**. As a result of this motional averaging, the linewidths narrow and the peaks move toward the center of the spectrum. In fact, at the rapid limit the spectrum has a lineshape and peak positions characteristic of a single orientation with

$$g = 1/3(g_x + g_y + g_z)$$

$$T = 1/3(T_x + T_y + T_z)$$

As the motion slows toward the rigid limit of conventional EPR (10^{-6} s) the effect of motion is two fold. First, there is motional averaging of g and T, though not complete averaging as in the case of sub nanosecond motion. Second, as the motion of the spin label is slowed it is able to move on and off resonance which manifests as enhanced relaxation which increases linewidth. Therefore, for a randomly oriented sample, when the rotational motion slows (τ_R increases toward the rigid limit) the splitting increases and lines broaden. These effects are shown in **Figure 11** and **Figure 22**, and spectral features can be used to measure τ_R in the 10^{-11} – 10^{-6} s range. For this work, we are interested in changes in dynamics and the nanosecond to millisecond timescale, and for this STEPR is used.

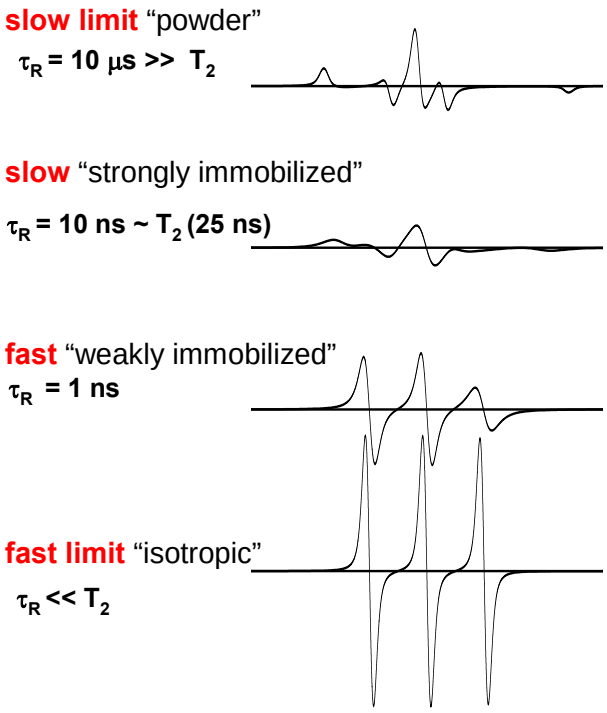

Figure 11 Dynamics, conventional EPR.
Simulated spectra showing the sensitivity of conventional EPR to the rate of rotational dynamics. Spectra as simulated assuming isotropic diffusion. Adapted from Dave Thomas Spectroscopy lecture.

2.7.2 Saturation Transfer EPR (STEPR)

STEPR spectra are often referred to as V_2'. V indicates that measurements are done in absorption mode. The "2" subscript indicates that ν_m = 50 kHz, with the phase-sensitive detection at 100 kHz (second harmonic). The prime (′) indicates that the spectrum is 90° out of phase, meaning the modulation phase $\phi_m = 90^o$ (minimum signal at nonsaturating power). A key parameter in STEPR is the microwave power. As indicated by the name Saturation Transfer, a saturating microwave power is used. Specifically the microwave power is set such the microwave magnetic field amplitude H_1 is 0.25 G (5,23) (see CHAPTER 3 for more details on STEPR).

Using the parameters highlighted above, the EPR experiment is setup such that the spectrum (V_2') is sensitive to rotational motions with τ_R comparable to the spin-lattice relaxation time T_1 (~ 11 μs) (**Figure 12**, A). When rotational motion is on the timescale of T_1 (τ_R in the μs to ms timescale), saturation appears to decrease. This is not because the motion is actually changing T_1, but the rotational motion decreases saturation by transferring it away from resonance. The intensity of the STEPR spectrum ($\int V_2'$) can then be used to determine τ_R (**Figure 12**, B). Though the theory and setup for a STEPR experiment may seem abstract, Squier and Thomas (23) provide a brief and useful description that summarizes the basic idea nicely.

"In general, a saturation transfer EPR experiment is one designed to detect the decreased saturation caused by microsecond rotational motions. The development of ST-EPR methods is thus primarily the development of spectral detection and display methods that are optimally sensitive to saturation, preferably in a way that maximizes motional effects and minimizes others."

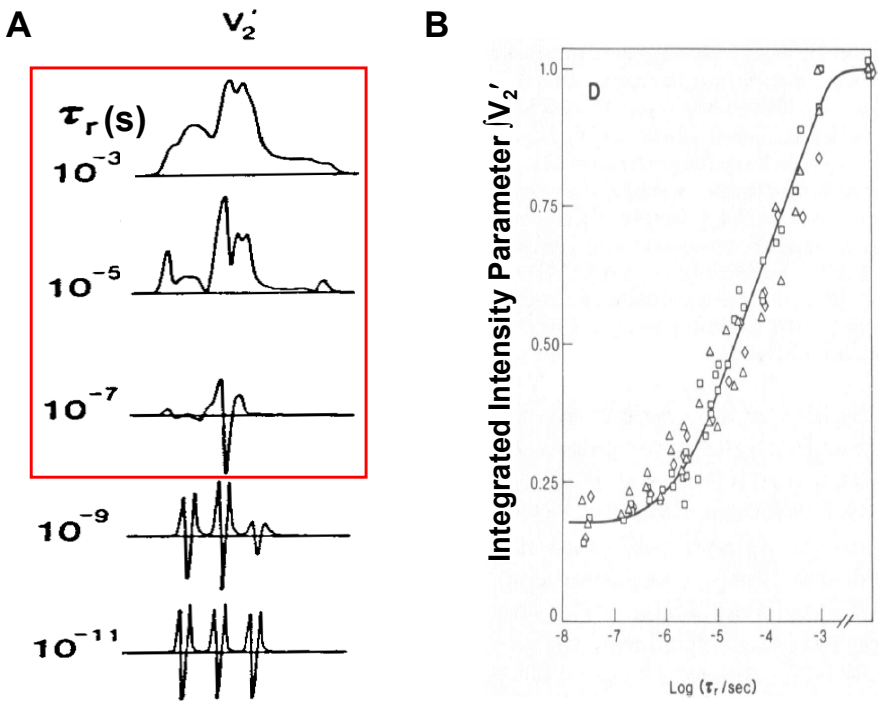

Figure 12 Dynamics, saturation transfer EPR.
A: Dependence of saturation transfer EPR spectra (V_2') on isotropic rotational correlation time. Red box indicates sensitive range of STEPR. Adapted from (24). B: Relationship between the integrated intensity parameter $\int V_2'$ and rotational correlation time τ_R. Adapted from (23).

2.8 Fitting EPR Spectra

In this work, spectral fitting was used to determine the orientational distribution of a spin label relative to the external magnetic field H. Using spin labels that are coupled to the peptide backbone made it possible to focus on protein orientation, and not probe dynamics. The probes used in this work have restricted nanosecond motions (though some are more restricted than others as seen in Chapters 3 and 4), meaning they are coupled to the protein backbone. Additionally, the highly organized structure of the muscle fiber bundle was taken advantage of by orienting the long-axis of the fiber bundle (which is synonymous with the actin filament axis) either parallel or perpendicular to H.

This section covers the basic principles and method used in simulating spectra from spin-labeled myosin on actin.

Simulating EPR spectra is a nontrivial process. There are numerous parameters, and some assumptions that need to be made. As mentioned above (eq. 2.4), the resonant condition is a function of the orientation of the nitroxide group in the magnetic field, described by the angles θ and ϕ. Therefore, a spin with a defined orientation will give rise to a spectrum with a specific center and splitting. When a nitroxide spin label is rigidly attached to myosin there is an orientational distribution of spins. One way to model this orientational distribution is a sin-weighted Gaussian with a width (full width at half-maximum) $\Delta\theta$ and center θ_0.

$$\boldsymbol{\rho}(\theta) = (\sin(\theta))\ \exp[-(\ln 2)\{(\theta - \theta_0)/(0.5\Delta\theta)\}^2]$$

A similar expression is used to describe the distribution about ϕ. Therefore, the EPR spectrum is linear combination of spectra described the distribution $\rho(\theta,\phi) = \rho(\theta)\rho(\phi)$. Relaxation processes and inhomogeneities in local spin environments also broaden the EPR spectrum. The EPR lineshape due to this broadening is often modeled as the first derivative of a Lorentzian function (25):

$$Y(H) = \frac{(H - H_{res})\Delta H_{pp}}{\left[(H - H_{res})^2 + \Delta H_{pp}^2\right]^2} \qquad \textbf{[eq. 2.5]}$$

where the peak-to-peak width (ΔH_{pp}) of the Lorentzian is defined by the spin-spin relaxation time T2:

$$\Delta H_{pp} = 2/(3^{1/2}\gamma T_2)$$

A simulated EPR spectrum can them be generated by integrating **eq. 2.5**, weighted by the orientational distribution of θ and ϕ, over all space:

$$V_l(H) = \iint Y(H,\theta,\phi,m_i)\rho(\theta,\varphi)\sin(\theta)\, d\theta d\phi \qquad \textbf{[eq. 2.6]}$$

For this work, the goal of fitting an EPR spectrum is to determine the orientational distribution of the spin label $\rho(\theta,\phi)$. To do this, different values of θ_0, $\Delta\theta$, ϕ_0 and $\Delta\phi$ are assumed, and the spectrum is then simulated using **eq. 2.6**, and compared to the experimental spectrum. However, this is a bit of an over simplification, there are some orientational independent parameters that must be determined first. Recall that H_{res} is a function of g and T, where:

$$g(\theta,\phi) = g_x\sin^2\theta\cos^2\phi + g_y\sin^2\theta\sin^2\phi + g_z\cos^2\theta$$

$$T(\theta,\phi) = (T_x^2\sin^2\theta\cos^2\phi + T_y^2\sin^2\theta\sin^2\phi + T_z^2\cos^2\theta)^{1/2}$$

The values g_x, g_y, g_z, T_x, T_y and T_z are independent of θ and ϕ, and need to be determined before fitting the oriented spectrum to determine $\rho(\theta,\phi)$. To determine these values, we need sample that is independent of orientation. Such a sample was obtained by mincing a fiber bundle. The minced spectrum was then simulated assuming $\Delta\theta = \Delta\phi \geq 90^o$, and letting g_x, g_y, g_z, T_x, T_y and T_z vary until best fit was achieved. The spectra of oriented fiber bundles could then be fit using these values and varying $\rho(\theta,\phi)$. A similar approach to spectral fitting has been used before (5,20,25-27).

Chapter 3: Three Distinct Actin-attached Structural States of Myosin in Muscle Fibers

Ryan N. Mello and David D. Thomas*

Department of Biochemistry, Molecular Biology and Biophysics, University of Minnesota, Minneapolis, Minnesota

Published in the *Biophysical Journal, 2012*

3.1 Overview

We have used thiol crosslinking and EPR to resolve structural transitions of myosin's light chain and catalytic domains (LCD, CD) that are associated with force generation. Spin labels were incorporated into the LCD of muscle fibers by exchanging spin-labeled regulatory light chain (RLC) for endogenous RLC, with full retention of function. To trap myosin in a structural state analogous to the elusive post-hydrolysis ternary complex A.M′.D.P, we used pPDM to crosslink SH1 (Cys707) to SH2 (Cys697) on the CD. LCD orientation and dynamics were measured in three biochemical states: relaxation (A.M.T), SH1-SH2 crosslinked (A.M′.D.P analog), and rigor (A.M.D). EPR showed that the LCD of crosslinked fibers has an orientational distribution intermediate between relaxation and rigor, and saturation transfer EPR revealed slow rotational dynamics indistinguishable from that of rigor. Similar results were obtained for the CD using a bifunctional spin label to crosslink SH1-SH2, but the CD was more disordered than the LCD. We conclude that SH1-SH2 crosslinking traps a state in which both the CD and LCD are intermediate between relaxation (highly disordered and microsecond dynamics) and rigor (highly ordered and rigid), supporting the hypothesis that the crosslinked state is an A.M′D.P analog on the force generation pathway.

3.2 Introduction

Muscle contraction is driven by the actin-activated hydrolysis of ATP by myosin, resulting in the relative sliding of actin and myosin filaments. Current mechanistic models propose

that filament sliding is driven by a structural transition of the myosin catalytic domain (CD) from a dynamically disordered state of weak actin binding to an ordered state of strong actin binding, and a lever arm rotation of the light-chain domain (LCD)(6-9). In the lever arm model, the LCD behaves as a semi-rigid rod that amplifies and propagates the force-producing structural changes in the myosin CD to the thick filament core (7,10). The strongly bound actomyosin complexes (A.M or A.M.D) are quite stable and have been studied in great detail, with EPR revealing that the orientations of the CD (28,29) and LCD (20,30) are well defined with respect to the actin filament axis. However, much less is known about the weakly bound complexes (A.M.T or A.M.D.P), which are more difficult to study due to their dynamic disorder and short lifetimes. Saturation transfer EPR (STEPR), with spin labels on the CD of myosin, in the steady state of ATP hydrolysis (31,32) or in the presence of ATPγS (11,33), has shown that weakly attached myosin heads undergo large-amplitude rotations with correlation times (τ_R) in the range of 1 – 20 μs. This dynamic disorder is consistent with the disordered appearance of myosin subfragment 1 (S1) bound to actin in electron micrographs of similar weakly bound complexes (34-36).

These spectroscopic and electron microscopic observations of weakly bound actomyosin complexes were done under conditions in which the predominant actin-attached myosin biochemical state was probably the prehydrolysis complex (A.M.T). However, the post hydrolysis ternary complex (A.M.D.P) is also of great interest, since there is evidence that force generation begins in this biochemical state, before phosphate is released but after isomerization to A.M′.D.P (15,16). This early-force complex has remained elusive, because actin (a) greatly accelerates the rate of P_i release, thus quickly

converting A.M′.D.P to A.M.D, and (b) shifts the equilibrium constant for hydrolysis toward the prehydrolysis state by a factor of 20 (17). Thus, preparation of a stable post-hydrolysis ternary complex or analog is crucial for understanding myosin's force-producing structural transitions. The post hydrolysis analogs ADP.V_i and ADP.AlF_4 would seem to provide an attractive approach to trapping the elusive A.M.D.P complex, but actin rapidly dissociates these phosphate analogs from myosin (37,38). The nucleotide analogs AMPPNP and pyrophosphate do remain bound in the ternary complexes with actin and myosin, but these complexes are structurally indistinguishable from the strongly bound complex A.M.D (33,39,40).

There are two proposed stable analogs of the ternary complex A.M′.D.P: the complex of actin with myosin, blebbistatin, and ADP (41) and the complex of actin with myosin that has been crosslinked with pPDM. In the present work, pPDM crosslinking was used to trap a stable analog of the A.M′.D.P state. pPDM specifically crosslinks the two most reactive cysteine residues, SH1 (Cys707) and SH2 (Cys697), on the CD of myosin (42-44). Several mechanical and biochemical studies have characterized pPDM-crosslinked myosin as a weak-binding state. Muscle fibers treated with pPDM exhibit an 85% decrease in isometric force (45) and a decrease in rigor stiffness to the level of resting untreated fibers (46). The actin-activated ATPase of pPDM-S1 is 0.2% of the rate of unmodified S1(42), and pPDM-S1 exhibits weak actin binding, with an actin affinity at low ionic strength (K_d = 30μM) ~ 3 times stronger than S1.ATP, 100 times weaker than S1.AMPPNP, and 1000 times weaker than S1.ADP (43). However pPDM-myosin does not trap nucleotide when bound to actin, as might be expected for a stable analog of the A.M′.D.P complex (42). Rather, pPDM

appears to trap the stable A.M′.D.P complex by trapping a structural state in which the SH1 helix is disordered (see Discussion, "Structural coupling within myosin").

Recent work using a bifunctional spin label (BSL), rather than pPDM, to crosslink SH1 to SH2 has characterized the orientation and dynamics of the BSL-S1 actin complex (5) (**Figure 13**). EPR of BSL-S1 bound to oriented actin in muscle fibers yields spectra characteristic of nearly random orientation, in contrast to the high degree of orientational order of S1 strongly bound to actin. However, STEPR of BSL-S1 reveals rotational dynamics with a correlation time (τ_R) ~ 600 μs, which is similar to that observed for the strongly bound biochemical states A.M and A.M.D, and 30 times slower than the weakly bound ternary complex A.M.T (33). It is evident that SH1-SH2 crosslinked myosin exhibits

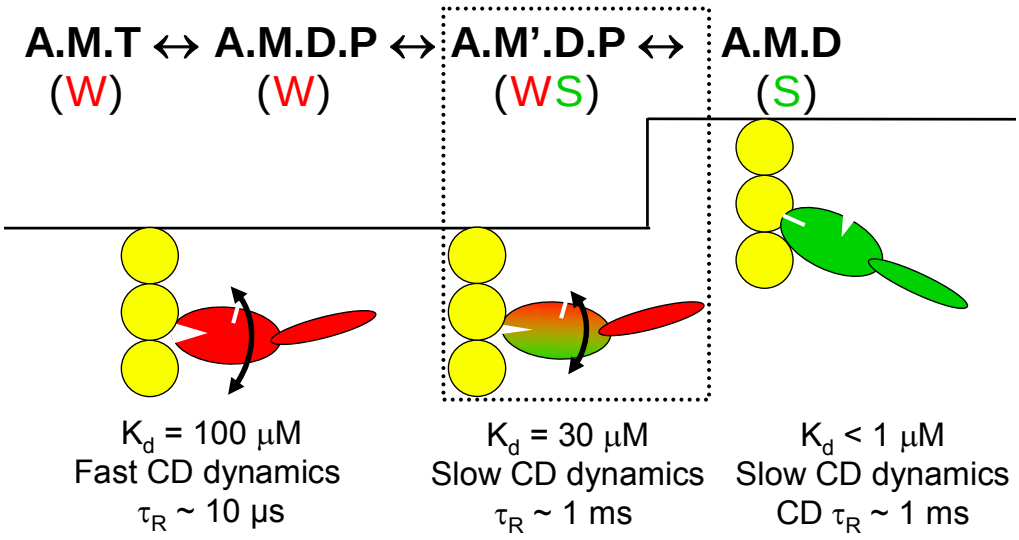

Figure 13 Model for coupling of actomyosin ATPase to force and movement.
This model focuses on the coupling of biochemical transitions to orientation and dynamics of the myosin catalytic domain, adapted from (7). Red and green signify weak (pre-force) and strong (force-bearing) complexes respectively, curved arrows signify orientational disorder, and an upward step indicates the power stroke. Text at top indicates the biochemical state (defined by the active site ligand): A, actin; M, myosin; T, ATP; D, ADP; P, inorganic phosphate. Prime (′) indicates a second structural state corresponding to the same biochemical state. Text under each state indicates distinguishing properties of the catalytic domain.

distinct structural properties that place it intermediate between A.M.T and A.M.D, as expected for an analog of the A.M′.D.P complex (**Figure 13**).

The spectroscopic results from BSL-S1, summarized above, provided new insight into the structural consequences of SH1-SH2 crosslinking. However, they were acquired with probes attached only on the CD of isolated S1, leaving two questions open: First, are the structural dynamics of crosslinked S1 due to orientational disorder of the entire myosin head, or to disorder within the head? Second, are these results characteristic of intact myosin in a muscle fiber? In muscle fibers, the myosin head is constrained not only by actin but also by the thick filament backbone. The resulting mechanical strain may limit the conformation of myosin as it binds actin, or dissociate a fraction of the heads due to weakened actin binding induced by crosslinking. To answer these questions, we used EPR to measure orientation and dynamics of both the LCD and CD in intact myosin in skinned skeletal muscle fibers. LCD measurements were made in three biochemical states: relaxation (A.M.T), pPDM-crosslinked (A.M′.D.P), and rigor (A.M.D). LCD orientation and dynamics in muscle fibers were measured by spin labeling purified RLC, then exchanging it with the endogenous RLC, with retention of muscle function. The CD was studied in crosslinked fibers, using BSL to simultaneously crosslink and spin-label the myosin CD.

3.3 Methods

Muscle fiber preparation and characterization

Glycerinated rabbit psoas muscle fiber bundles were prepared and stored in a solution containing 1:1 mixture of rigor solution (60 mM KPr, 2 mM $MgCl_2$, 1 mM EGTA, 25 mM MOPS, pH 7.0, 25^o C) and glycerol at -20^{o}C for up to 6 months without significant loss of function (47). Chicken gizzard RLC was prepared and labeled with FDNASL as described in the Supplementary Material Section 1. Spin-labeled RLC (FDNASL-RLC) was then exchanged for endogenous RLC in fiber bundles (Supplementary Material, Section 3). The extent of RLC extraction and reconstitution was determined by densitometric analysis of SDS-PAGE on fiber homogenates (Supplementary Material, Section 4). Muscle fiber function after RLC exchange was assessed by measuring the Ca dependence of myofibrillar MgATPase activity (Supplementary Material, Section 5).

Crosslinking with pPDM and BSL

SH1 (Cys707) and SH2 (Cys697) were crosslinked using pPDM (Sigma-Aldrich, St. Louis, MO), using the same setup used for RLC exchange (Supplementary Material, Section 3) except that temperature was always 4^{o}C. The fiber bundle was washed for 15 minutes with crosslinking solution (190 mM KPr, 2 mM MgCl2, 1 mM EGTA, 20 mM MOPS, 5 mM MgATP), and pPDM (in dimethylformamide) was added to crosslinking solution such that the final [pPDM] was 200 μM and dimethylformamide never exceeded 1%. After 75 minutes, the fiber bundle was washed with RS190 (crosslinking solution without MgATP) for 15 minutes to remove unreacted pPDM and MgATP. K/EDTA and

Ca/K ATPase activities (Supplementary Material, Section 5) were used to determine the extent of pPDM crosslinking. SH1 and SH2 were also crosslinked with the bifunctional spin label 3,4-Bis-(methanethiosulfonylmethyl)-2,2,5,5-tetramethyl-2,5-dihydro-1H-pyrrol-1-yloxy Radical (BSL) (Toronto Research Chemicals, North York, ON). The experimental setup and BSL crosslinking procedure was identical to that used for crosslinking with pPDM, except that the BSL concentration was 100 μM and the reaction time was 75 minutes.

EPR spectroscopy

EPR spectra were recorded at X-band (9.5 GHz) with a Bruker (Billerica, MA) E500 spectrometer, using either a TE_{102} (Bruker 4104OR-R) or TM_{110} (Bruker 4103TMA) cavity. The sample temperature was maintained at 23°C by flowing temperature-controlled N_2 gas through a nozzle attached to the optical port on the front of the cavity (TE_{102}) or a quartz dewar inserted into the bottom of the cavity (TM_{110}). The sweep width was 120 G (1024 points), sweep time was typically 41.94 s (conversion time 40.96 ms), and the center field value H_C was set proportionally to the microwave frequency ν (H_C = ν/2.803 MHz/G, corresponding to a g value of 2.0027, the value of g_z for a typical nitroxide) so that all spectra were equivalently aligned. For EPR experiments on oriented muscle fiber bundles under perfusion, the procedure was essentially the same as that used during RLC exchange (Supplementary Material, Section 3). The solution flow rate varied from 115 μL/min to 340μL/min, such that a further increase in flow rate did not affect the spectra.

EPR spectra were acquired in either RS190 (190 mM KPr, 2 mM $MgCl_2$, 1 mM EGTA, 20 mM MOPS, pH 7.0) or in relaxation solution (RS190 with 20mM KPr rather than 190 mM KPr, plus 5 mM MgATP, 50 mM creatine phosphate, and 750 units/ml of creatine phosphokinase) (48). Ionic strength was 203 mM for both solutions. Spectra of RLC-labeled fibers in rigor and pPDM-crosslinked states were acquired while perfusing the fiber with RS190, and relaxation spectra were acquired while perfusing relaxation solution. Spectra of BSL-fibers were also acquired while perfusing the fibers with RS190, in order to remove free spin label that was slowly released. For EPR experiments on randomized samples, fibers in RS190 were minced with a razor blade and placed in a quartz flat cell that contained a well of dimensions 0.5 x 1.0 x 0.05 cm (WG-806-Q, Wilmad-Labglass, Buena, NJ). Excess moisture was wicked away and a coverslip was placed over the sample well and sealed with Parafilm M (Pechiney Plastic Packaging Company, Chicago, IL) to prevent sample dehydration. The flat cell assembly was centered in the EPR cavity with its face oriented parallel or perpendicular to the applied magnetic field.

Conventional spectra (V_1) of RLC-labeled fibers and BSL-fibers were acquired with the long axis of the fiber bundle oriented either parallel (using a modified TM_{110} cavity (20)) or perpendicular (using a TE_{102} cavity) to the applied magnetic field. Microwave power was set from 20 mW to 32 mW, to maximize the signal intensity without causing significant saturation. The modulation frequency was 100 kHz (first harmonic), and the peak-to-peak modulation amplitude was 2 G. The filter time constant was set equal to the conversion time (40.96 ms). Spectra of fibers were analyzed to

determine the orientational distribution of the spin label relative to the muscle fiber axis, using computational simulation and least-squares minimization (5,26,28). Briefly, the spectrum of minced fiber bundles was fit to obtain the orientation-independent parameters, including the anisotropic T and g tensors and the linewidths. Spectra of oriented fiber bundles were then fitted to determine the orientational distribution of the spin label relative to the fiber axis, defined by the center (θ_0') and the width ($\Delta\theta'$, full width at half maximum) of the assumed Gaussian orientational distribution. Analysis of the spectrum from minced RLC-labeled fibers indicated two components with different tensor values. One component, having a wider splitting than the predominant component, composes a small fraction (≤ 0.15) of the total spectrum and presumably represents a small fraction of nonspecifically bound RLCs. Previously, this nonspecific component comprised 40% of the spectrum (20). This small nonspecific component was digitally subtracted before fitting.

Saturation transfer EPR spectra (V_2') of RLC-labeled fibers and BSL-fibers were acquired as described previously (5,23). Fibers were aligned perpendicular to the field in order to minimize the effects of orientation on the spectrum. In STEPR, the microwave power P is set such that the microwave field amplitude H_1 is 0.25 G, determined from $P = (H_1^2/K)(Q_0/Q)$, where K is determined by calibration with a sample of known saturation properties (23), Q_0 is the cavity quality factor (measured by the spectrometer) during the calibration, and Q is the value measured for each experiment. For the muscle fiber setup used in the present work, K was typically measured to be 1.06 G^2/W and $Q_0 = 3000$, so P was typically set at 59 mW x 3000/Q for STEPR. The following parameters were used to

acquire V_2': H_1 = 0.25G, modulation frequency ν_m = 50 kHz with the phase-sensitive detection at 100 kHz (second harmonic), peak-to-peak modulation amplitude H_m = 5.0 G, modulation phase $\phi_m = 90^o$ (minimum signal at nonsaturating power), filter time constant = 328 ms. V_2' spectra were analyzed to determine the rotational correlation time τ_R, based on the integrated intensity parameter $\int V_2'$, which is independent of the spin concentration and orientation (23).

3.4 Results

RLC Exchange

Previous work using EPR to measure LCD orientation indicates a large population of RLC bound nonspecifically in skeletal muscle fibers (Supplementary Material, Section 2) (20,30,49). Using a modified RLC exchange method (Supplementary Material, Section 3), we minimized this population of nonspecific RLC to < 15% of the total spin-labeled RLC (**Figure 19**), a substantial improvement compared to previous EPR studies (20). The extent of RLC extraction and reconstitution (**Figure 20**) indicated that 54 ± 10 % of the endogenous RLC was exchanged with spin-labeled RLC. Muscle function after RLC exchange was normal, as shown by the Ca dependence of myofibrillar MgATPase (**Table 1**). This improvement in RLC exchange technology, compared to previous EPR studies on skeletal muscle fibers (20,30,49), dramatically enhances the sensitivity and validity of LCD structural measurements.

Crosslinking SH1 and SH2 with pPDM

K/EDTA-ATPase and Ca/K-ATPase activities were used to determine the extent and specificity of SH1-SH2 modification with pPDM. ATPase measurements from control (no pPDM) and pPDM-treated fibers are summarized in **Table 1**. Both the K/EDTA- and Ca/K-ATPase are inhibited by pPDM treatment (**Table 1**). As shown previously (5), these values indicate that at least 90% of the myosin heads were modified at SH1 and SH2, presumably due to crosslinking by pPDM. We can not rule out the possibility that some of the effects are due to modification of other thiols, including those on actin, tropomyosin, and troponin. However, previous studies have shown that reaction of skinned fibers with thiol-reactive probes under these conditions is remarkably specific for SH1, and that the reaction of BSL with myosin S1 is quite specific for SH1-SH2 (5), so it is likely that most of the reaction of pPDM and BSL is with SH1 and SH2.

Table 1 ATPase assays

Sample	MgATPase V_{max}	MgATPase pK_{Ca}	K/EDTA-ATPase	Ca/K-ATPase
Control	0.322 ± 0.021	5.87 ± 0.01	0.459 ± 0.021	0.066 ± 0.013
RLC exchanged	0.321 ± 0.024	5.83 ± 0.09	-	-
pPDM crosslinked	-	-	0.0508 ± 0.013	0.038 ± 0.024

All values are reported as mean ± SEM (n = 4-6). V_{max}, K/EDTA-ATPase, and Ca/K-ATPase values have units of μmol/mg protein/min. Control fibers underwent a mock RLC exchange or mock pPDM treatment.

LCD orientation measured by conventional EPR

EPR is extremely sensitive to the orientational distribution of a spin label with respect to the applied magnetic field (H). At the frequency used here (X-band, 9.5 GHz) EPR is

primarily sensitive to the angle θ between the spin label's principal axis and H. In a well-oriented muscle fiber, aligned either parallel or perpendicular to H, the EPR spectrum detects directly the angle θ′ between the spin label's principal axis and the fiber axis (Fig. S3) (28). Thus the recording of parallel and perpendicular spectra provides a clear graphical indication of the degree of orientation of the spin label relative to the fiber axis. The parallel spectrum is then analyzed to determine the precise orientational distribution ρ(θ′).

LCD orientation, with respect to the fiber axis, was determined from conventional EPR spectra (V_1) of spin-labeled RLC in skinned muscle fiber bundles. Parallel and perpendicular spectra of minced fiber bundles are nearly identical, indicating random orientation (**Figure 14**, top). EPR spectra of oriented fiber bundles were acquired in three different biochemical states: relaxation (A.M.T, pre-power stroke), rigor (A.M.D, post-power stroke) and SH1-SH2 crosslinked with pPDM (A.M′.D.P) (**Figure 14**). In relaxation, spectra are nearly independent of fiber orientation, indicating virtually random orientation of the LCD ($\theta_0' = 72^o \pm 9^o$, $\Delta\theta' = 89^o \pm 11^o$). In rigor, the spectra are quite sensitive to fiber orientation, indicating a single population with a high degree of orientational order ($\theta_0' = 41^o \pm 4^o$, $\Delta\theta' = 38^o \pm 6^o$). After pPDM treatment, sensitivity to fiber orientation is intermediate between that of relaxation and rigor ($\theta_0' = 54^o \pm 6^o$, $\Delta\theta' = 64^o \pm 16^o$). We conclude that in relaxation (A.M.T, pre-power stroke) the LCD is randomly disordered, in rigor (A.M.D, post-power stroke) the LCD is highly ordered, and in the pPDM crosslinked state (analog of A.M′.D.P) the LCD is partially disordered, with an orientational distribution intermediate between those of relaxation and rigor. However,

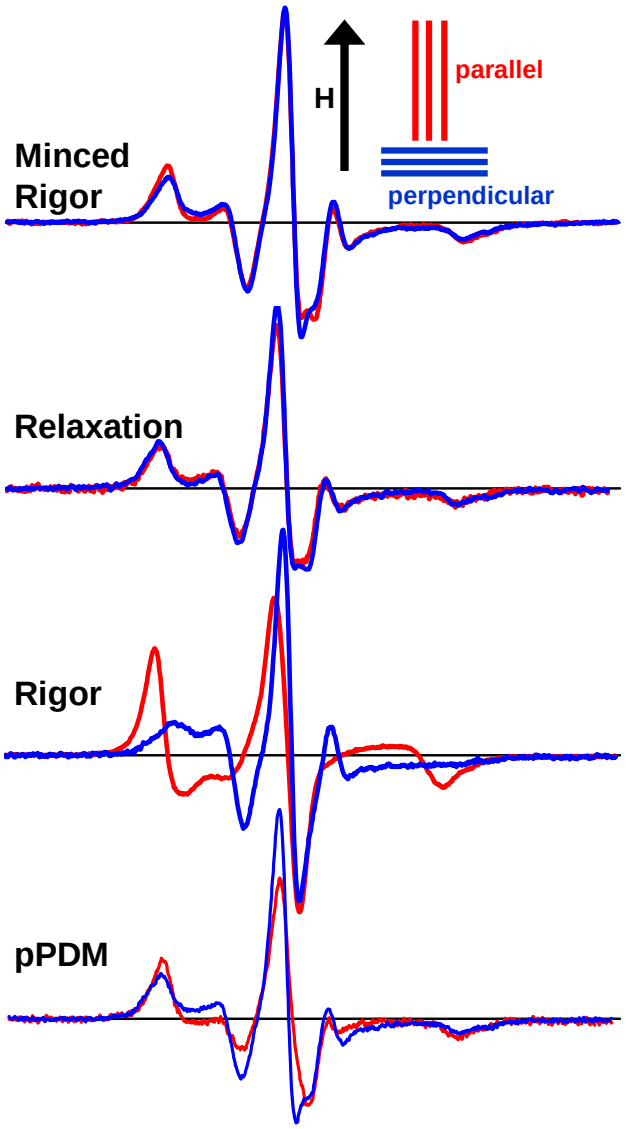

Figure 14 Conventional EPR spectra (V_1) of spin-labeled LCD.
Spectra were acquired with the flat cell (top) or the capillary containing oriented fibers (bottom three) oriented parallel (red) or perpendicular (blue) to the magnetic filed **H**. The buffer was either RS190 (rigor, pPDM) or relaxation solution (see 2.3 METHODS).

this amount of disorder is enough that we can not determine whether there is a single disordered population or a mixture of ordered and disordered populations.

Based on conventional EPR spectra (**Figure 14**), the intermediate orientation of the LCD in pPDM crosslinked fibers can be explained by two distinct models. In model 1 (**Figure 15**, left) crosslinking traps a state in which both myosin heads are bound to actin with static orientational disorder that is intermediate between relaxation (A.M.T.) and

rigor (A.M.D). In model 2 (**Figure 15**, right), crosslinking traps a state in which half of the heads are dissociated from actin (and dynamically disordered as in relaxation) while the other half remain strongly bound as in rigor, as observed previously for the nucleotide analogs PP_i and AMPPNP (39,40). It has been shown previously that both the CD (31,32,50) and LCD (51,52) of dissociated heads are dynamically disordered, with a rotational correlation time $\tau_R \sim 10$ μs. Thus to decide between the two models in **Figure 15**, we must measure the rotational correlation time τ_R, to determine whether the disorder is static (Model 1) or dynamic (Model 2) on the microsecond time scale. This calls for saturation transfer EPR (STEPR).

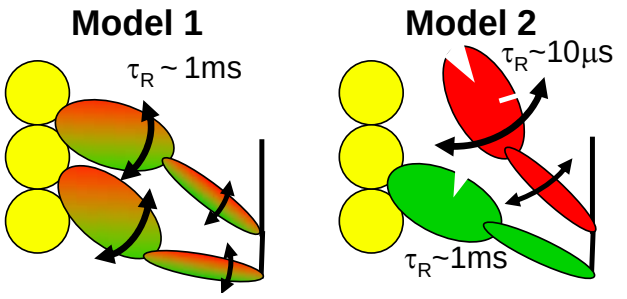

Figure 15 Structural models based on EPR spectra. The two models represent alternative hypothesis consistent with the conventional EPR spectra of pPDM-treated fibers (**Figure 14**, bottom).

RLC dynamics measured by STEPR

In addition to being sensitive to orientation, EPR is sensitive to rotational dynamics (Fig. S4), but conventional EPR (V_1) is sensitive to rotational motion only for rotational correlation times (τ_R) in the picosecond-to-microsecond time range, so it is not sensitive to the slow rotational dynamics of large proteins such as myosin (7). Therefore, we must use STEPR (V_2'), which is sensitive to the microsecond-to- millisecond time range (53).

STEPR was used to detect the microsecond rotational dynamics of LCD in relaxation, rigor, and the pPDM crosslinked state (**Figure 16**, bottom). Rotational

correlation times were determined from STEPR spectra (V_2') using the integrated intensity parameter ($\int V_2'$) as described in METHODS (23). It is clear that the spectrum obtained in relaxation is much less intense than the other two cases (rigor and crosslinked), which are essentially identical. The values of $\int V_2'$ (**Figure 16**, inset) in relaxation, rigor, and the crosslinked state are 0.54 ± 0.026, 1.01 ± 0.047, and 0.96 ± 0.064, respectively, corresponding to τ_R values of 22 ± 3.6 μs in relaxation and ≥ 1ms for both rigor and pPDM (23). We conclude that the rotational dynamics of LCD in the pPDM-crosslinked state (analog of A.M′.D.P) is indistinguishable from that of rigor (A.M.D), and much slower than in relaxation (A.M.T), despite the orientational distribution being intermediate between relaxation and rigor (**Figure 16**, top). These results are consistent with Model 1 but not Model 2 (**Figure 15**). Crosslinking traps a state in which both heads are bound to actin with static orientational disorder.

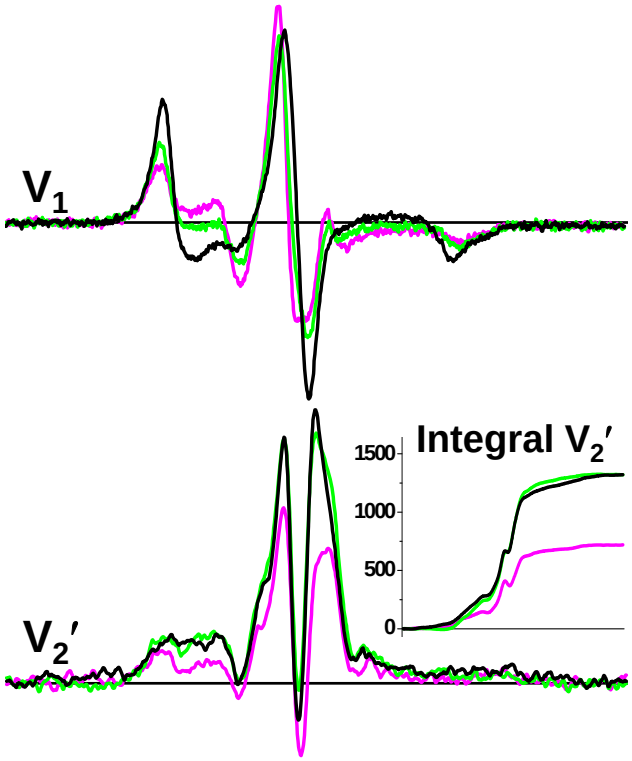

Figure 16 Effect of pPDM crosslinking on EPR spectra of spin-labeled myosin LCD. Spectra were acquired in relaxation (magenta), rigor (black), and the pPDM crosslinked state (green). Top: Conventional EPR of fibers oriented parallel to the field (V_1 from **Figure 14**). Bottom: STEPR spectra (V_2') of fibers oriented perpendicular to the field. Inset shows $\int V_2'$. The buffer was RS190 (rigor and pPDM) or relaxation solution (3.3 METHODS).

Catalytic domain orientation and dynamics of BSL-fibers

Isolated BSL-S1 bound to actin in oriented muscle fibers is almost randomly oriented and exhibits slow rotational dynamics ($\tau_R \sim 600$ μs), similar to that of rigor and 30 times slower than observed for the ternary complex A.M.T (5,33). However, it is possible that the head of endogenous myosin behaves differently due to restriction by the thick filament backbone. Thus, to gain more complete understanding of the complex trapped by SH1-SH2 crosslinking, we measured catalytic domain orientation and dynamics in crosslinked fibers, using BSL to simultaneously crosslink and spin label myosin.

Conventional EPR spectra of BSL-fibers were acquired with the fiber axis parallel or perpendicular to the magnetic field H. Parallel and perpendicular spectra are nearly identical, indicating a highly, but not completely, disordered CD ($\theta_0' = 85^o \pm 3^o$, $\Delta\theta' = 77^o \pm 4^o$) (**Figure 17**, top). In contrast, previous EPR studies demonstrate that uncrosslinked fibers spin-labeled at SH1 exhibit a narrow angular distribution in rigor with $\Delta\theta' \sim 15^o$, and random orientation ($\Delta\theta' \geq 90^o$) in relaxation (28). Thus SH1-SH2 crosslinking produces an orientational distribution of the CD that is much more disordered than in rigor and slightly less disordered than in relaxation.

The STEPR spectrum of BSL-fibers (**Figure 17**, bottom) demonstrates extremely slow rotational dynamics of the CD, with $\int V_2' = 1.27 \pm 0.26$, corresponding to the rigid limit of STEPR ($\tau_R \geq 1$ ms). This result is similar to that of rigor, in which the CD is

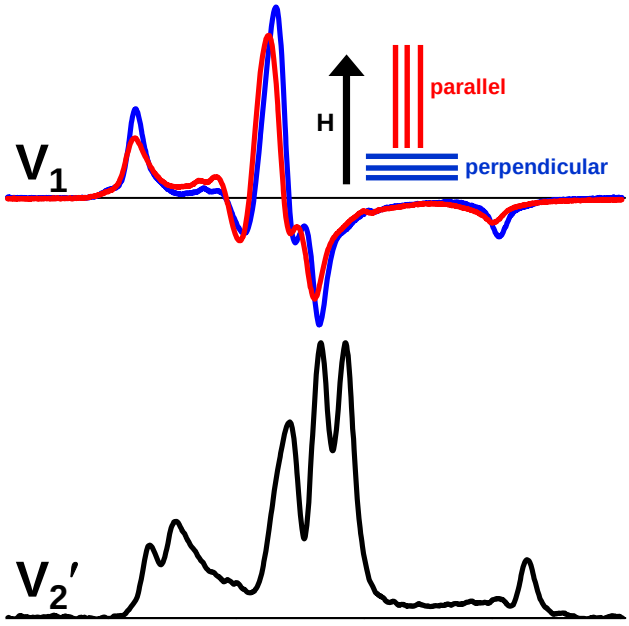

Figure 17 EPR spectra of skinned fiber bundles labeled on myosin CD with BSL.
BSL was used to spin-label myosin and crosslink SH1 and SH2. Top: conventional EPR (V_1) of fiber bundles, with the fiber axis oriented parallel (red) and perpendicular (blue) to the magnetic field H. Bottom: STEPR (V_2'). The buffer was RS190.

immobile on the microsecond timescale (50), and much slower than in relaxation ($\tau_R \sim 10$ μs) (31,32,50). We conclude that the CD in SH1-SH2 crosslinked fibers is much more disordered than in rigor, but not as disordered as in relaxation, and rotational motions are as slow as in rigor.

In comparing the LCD (**Figure 16**) with the CD (**Figure 17**), the crosslinked state in fibers has similar properties – highly disordered (as in relaxation) but static (as in rigor). However, the disorder of the LCD ($\Delta\theta' = 64^o$) is significantly less than that of the CD ($\Delta\theta' = 77^o$), suggesting that the source of disorder is at the actin-CD interface. In support of this hypothesis, the CD of BSL-fibers is not as disordered as the CD of BSL-S1 (5), indicating that CD disorder in intact myosin in fibers is restricted by connection to the thick filament backbone.

3.5 Discussion

Summary of results

We have used RLC exchange, myosin crosslinking, and EPR to measure the orientation and dynamics of myosin's LCD in three biochemical states, relaxation (A.M.T), SH1-SH2 crosslinked (A.M′.D.P analog), and rigor (A.M.D). Modification of a previously described RLC-exchange protocol (54) made it possible to reduce nonspecific RLC binding (Fig. S1) while replacing 54% of the endogenous RLC with spin-labeled RLC (Fig. S2), with retention of function as defined by the Ca-dependence of myofibrillar MgATPase (**Table 1**). Conventional EPR was used to measure the orientational

distribution of the LCD in RLC-exchanged muscle fiber bundles (**Figure 14**). In relaxation (A.M.T, pre-power stroke) the LCD is highly disordered, in rigor (A.M.D, post-power stroke) the LCD is orientationally ordered, and in the pPDM crosslinked state (A.M′.D.P) the LCD has an orientational distribution intermediate between relaxation and rigor. STEPR demonstrates that LCD dynamics in crosslinked fibers is indistinguishable from rigor ($\tau_R \geq 1$ ms) and much slower than in relaxation ($\tau_R = 22$ μs) (**Figure 16**). We also measured CD orientation and dynamics in fiber bundles crosslinked with BSL (**Figure 17**) and found that both conventional and STEPR results are similar to those of the LCD in crosslinked fiber bundles (**Figure 16**). The CD of SH1-SH2 crosslinked fibers is more disordered than in rigor, but not as disordered as in relaxation. The dynamics of the CD in SH1-SH2 crosslinked fibers is indistinguishable from rigor ($\tau_R \geq 1$ ms) and much slower than relaxation ($\tau_R \sim 10$ μs). Thus SH1-SH2 crosslinking disorders both the CD and LCD, but this orientational disorder is much less dynamic than in relaxation.

Interpretation of results

During the actomyosin ATPase cycle, myosin transitions from a disordered state of weak actin-binding to an ordered state of strong actin-binding (**Figure 1**). The weakly bound complexes (A.M.T) (11,31-36) and the strongly bound complexes (A.M and A.M.D) (20,28,29) have been the subject of many studies. However, relatively little is known about post-hydrolysis ternary complexes, especially the force-generating A.M′.D.P. There is one stable equilibrium complex proposed to be analogous to A.M′.D.P, namely, the complex of

actin with SH1-SH2 crosslinked myosin. Recent work on BSL-S1 showed that crosslinked S1 is orientationally disordered but has very slow rotational dynamics (5). However, since that work was done with probes attached on the CD of isolated S1, two questions remained open: First, are the structural dynamics of crosslinked S1 due to orientational disorder of the entire myosin head, or to disorder within the head? Second, are these results characteristic of intact myosin in a muscle fiber?

In the present study, the combination of conventional and saturation transfer EPR has answered these two questions. **Figure 14** and **Figure 16** demonstrate that crosslinking stabilizes a state in which the LCD has an orientational distribution intermediate between relaxation and rigor with dynamics that is static on the μs timescale, as shown previously for the CD (5). Thus, crosslinking disorders the entire actin-bound myosin head. The second question is answered by EPR spectra of BSL-fibers (**Figure 17**). Spectra indicate a large amount of orientational disorder ($\Delta\theta' = 77^{o}$) (**Figure 17**), but less than observed for actin-attached BSL-S1 ($\Delta\theta' \geq 90$) (5), and slow dynamics indistinguishable from rigor ($\tau_R \geq 1$ ms). This result is consistent with the hypothesis that the myosin head is constrained not only by actin but also by the thick filament backbone, and the resulting mechanical strain limits the conformation of myosin as it binds actin. These results indicate flexible structural-coupling between myosin's CD and LCD. That is, the structural transitions of myosin CD and LCD are similar throughout the actomyosin ATPase cycle, though not identical. It is remarkable that SH1-SH2 crosslinking on the distal CD has such a profound structural effect on the proximal LCD. However, the current work does not determine whether the LCD is acting as a semi-rigid rod to amplify the force-producing structural

changes in the CD, as proposed by the lever arm model (7,10), or the LCD merely follows the CD throughout its force-producing structural transitions.

We propose that crosslinking SH1 and SH2 traps an intermediate state that is minimally populated during the steady state of muscle contraction (A.M′.D.P), without trapping hydrolysis products. This is consistent with the small (often negligible) change in orientation between relaxation and contraction, as detected by spectroscopic probes on the myosin head, especially for LCD probes in skeletal muscle (20,30,49,55-57). Changes in CD orientation are usually more detectable, probably because the LCD is more flexible (38^{o} of disorder in rigor (**Figure 14**)) than the CD (15^{o} of disorder in rigor (29)). This emphasizes the importance of measuring LCD orientation and dynamics in stable states analogous to the A.M′.D.P state, and explains why the current work resolves three distinct structural states of the LCD.

Structural coupling within myosin

Function of the myosin CD requires coordinated movement of the four subdomains (upper 50 kDa, lower 50 kDa, N-terminal, and converter) coordinated with structural transitions in three flexible joints (switch II, relay helix, SH1 helix) (58-60). Previous biochemical work has shown that the SH1 helix becomes much more flexible upon nucleotide binding (61,62), and subsequent crystal structures suggested that nucleotide-induced unfolding of the SH1 helix uncouples the LCD and converter subdomain from the rest of the CD, producing an internally uncoupled state that allows increased motion of the converter and LCD and facilitates the transition to the pre-power stroke

conformation (58). These results explain SH1-SH2 crosslinking studies, showing that pPDM and other crosslinkers trap a weak-binding state of myosin in a nucleotide-dependent manner (62). Spin probes at SH1 indicate that both folded and unfolded states are populated, in a nucleotide-dependent equilibrium (63,64). Taken together, these results indicate that the SH1 helix has two structural states, folded and unfolded, that are loosely coupled to the biochemical state, as defined by the bound nucleotide. Only by crosslinking SH1 to SH2 (or by crystallizing myosin under special conditions) can the unfolded state be trapped. In the present study, we have exploited these principles to trap the myosin head in this weakly bound structural state on actin, and our EPR results support the proposal that the CD and LCD are partially uncoupled in this state. Measurements of myosin CD and LCD orientation and dynamics indicate that both domains exhibit increased disorder relative to relaxation (pre-power stroke) but slow dynamics indistinguishable from rigor (post-power stroke), and the structural properties of the two domains are distinct -- the CD is more disordered. This is consistent with the hypothesis that unwinding of the SH1 helix partially uncouples the LCD and CD (58,65), but it is notable that this uncoupling and the resulting increased freedom of the LCD results in rigor-like dynamics of the LCD ($\tau_R \geq 1$ ms), at least two orders of magnitude slower than observed for weak-binding states in the presence of ATP (11,31-33). The slow dynamics of the RLC in the crosslinked state correlates with the actin-binding properties of this state; pPDM-S1 binds actin ~ 3 time stronger than S1.ATP (43).

Though we speculate that the pPDM-crosslinked state is analogous to the A.M.D.P biochemical state, we do not propose that hydrolysis products are trapped in

this state. Rather, crosslinking traps myosin in a conformation that is populated after hydrolysis and isomerization to the A.M′.D.P state, but before product release and force generation. In addition to SH1-SH2 crosslinking, myosin complexed with ADP and the myosin inhibitor blebbistatin has been proposed to stabilize an analog of the A.M.D.P state (41). However, unlike crosslinking with pPDM, (a) ADP/blebbistatin is proposed to stabilize this pre-power stroke state by stabilizing the M.D.P complex and slowing P_i release (66), and (b) myosin complexed with ADP and blebbistatin retains high actin affinity (similar to M.ADP) and a primed (pre-power stroke) LCD position (41).

Conclusions

These structural measurements made on skinned muscle fibers are consistent with a revised model (**Figure. 18**) that is distinct from the previous model (**Figure 13**) for coupling of actomyosin ATPase to force and movement. We conclude that crosslinking traps myosin in a structural state that is intermediate between weak-binding states (clearly preceding the power stroke) and strong-binding states (clearly following the power stroke). Though this conclusion is speculative, it is supported by an abundance of evidence. Considered collectively, previous measurements on SH1-SH2 crosslinked myosin indicate mechanical and biochemical properties intermediate between weak- and strong-binding states. Mechanical measurements indicate that pPDM-treated fibers exhibit an 85% decrease in isometric force (45) and a decrease in rigor stiffness to the level of resting fibers (46). Biochemical studies demonstrate that pPDM-S1 exhibits actin binding 1000 times weaker than S1.ADP but ~ 3 times stronger that S1.ATP (43). The present work

demonstrates that the structural dynamics of this state is also intermediate between weak- and strong-binding states in a strikingly similar way as demonstrated in **Figure 14**, **Figure 16**, and **Figure 17**, and discussed below. We measured LCD orientation and dynamics in relaxation, the pPDM-crosslinked sate, and rigor (**Figure 14** and **Figure 16**), demonstrating that the LCD transitions from a highly disordered state with microsecond dynamics (A.M.T) to a slightly more ordered state that is static on the microsecond timescale (A.M′.D.P analog), to a highly ordered state that is also static on the microsecond timescale (A.M.D). This sequence of structural transition of the LCD is similar to the disorder-to-order transition of the CD (28,29,50), although the CD is more dynamically disordered than the LCD in both the A.M.T and A.M′.D.P states, and the LCD is more disordered than the CD in rigor (A.M.D). An important challenge for the future is to test the model in **Figure. 18** by observing the proposed intermediate not by trapping it, but by resolving it in the transient phase of a structural kinetics experiment (67).

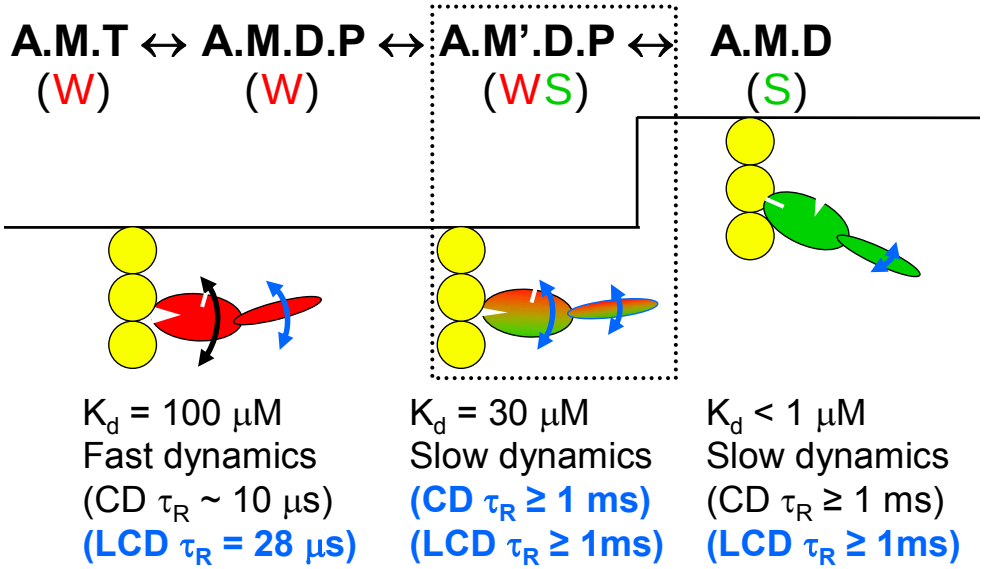

Figure. 18 Updated model for coupling of actomyosin ATPase to force.
Model is updated version of **Figure 13**. The text under each state indicates the distinguishing properties of the CD and LCD. Blue text and curved arrows denote revisions based on the current study.

3.6 Supplementary Material

The Supplementary Material Section includes five Sections and four figures.

Section 1: RLC preparation and labeling

Chicken gizzard RLC (cgRLC) was used because (a) mechanics is preserved when cgRLC is exchanged for endogenous RLC in skinned rabbit psoas muscle(68), and (b) cgRLC contains a single Cys that enables specific spin labeling. The cgRLC was expressed in *E. coli*, purified as described previously (69,70), labeled at Cys108 with the cysteine-specific spin probe FDNASL (20), dissolved in labeling solution (50 mM NaCl, 2 mM EDTA, 20 mM EPPS, pH 8.0), and treated with 5 mM DTT for 1.5 hours. DTT was removed using two Zeba spin columns (Thermo Fisher Scientific Inc., Rockford, IL),

protein concentration was adjusted to 100 μM, spin label was added at 500 μM, and the sample was incubated for 18-22 h on ice. Unreacted spin label was removed with a spin column equilibrated with Mg wash solution (40 mM NaCl, 2 mM $MgCl_2$, 10 mM EPPS, pH 8.0). If the FDNASL-RLC was not used within 1 day it was stored at -80^{o}C with 15% glycerol by volume. To simplify nomenclature, cgRLC is referred to as RLC in all other sections, other types of RLC are identified explicitly, and cgRLC labeled with the spin probe FDNASL is referred to as FDNASL-RLC.

The extent of spin labeling (spin labels per RLC) was determined both by digital analysis of EPR spectra (71) and by electrospray mass spectrometry (70). Briefly, for EPR analysis, the double integral of the V_1 spectrum of a known concentration of RLC (50 - 150 μM) was obtained at sufficiently low power to avoid saturation (typically < 1 mW). This value was then compared to the double integral of a sample of known spin label concentration (100 μM 2,2,6,6-Tetramethyl-1-piperidinyloxy (TEMPO)) at the same microwave power and H_1 value, to obtain the number of spin labels per RLC. For electrospray mass spectrometry, both unlabeled and labeled RLC (50 μM in 5mM ammonium bicarbonate solution) were injected into a QSTAR 2 quadrupole-TOF mass spectrometer with an electrospray ionization source. The resulting spectra were analyzed using Analyst QS software (Applied Biosystems). The area under peaks corresponding to unlabeled and labeled RLC were used to calculate the extent of spin labeling. The molar spin/protein ratio was 0.90 ± 0.08 determined from EPR analysis and 0.95 ± 0.01 determined from mass spectrometry, indicating essentially complete and specific reaction at Cys108.

Section 2: Nonspecific RLC binding

Previous work using EPR to measure LCD orientation indicated a significant fraction of nonspecific (largely disordered) RLC binding in skeletal muscle (20,30,49). We tested the hypothesis of nonspecific RLC binding in skeletal muscle fibers by incubating a fiber bundle in FDNASL-RLC, perfusing the fiber bundle with solution after incubation (to rinse away free FDNASL-RLC), and then using EPR to detect the presence of FDNASL-RLC. After rinsing away the free FDNASL-RLC, the fiber bundle had a significant EPR signal, V_{ns} (**Figure 19**, C). Since this fiber bundle did not have any of its native RLC extracted, and the EPR spectrum V_{ns} is indicative of random orientation, it is likely that the remaining exogenous FDNASL-RLC is bound nonspecifically. In an effort to minimize this nonspecifically bound RLC, we combined the RLC extraction and reconstitution steps. Previously, RLC extraction was followed by a separate reconstitution step (20,30,49,54). The purpose of combining the RLC extraction and reconstitution into one step is to extract the endogenous RLC and immediately replace it with FDNASL-RLC, while at the same time removing any FDNASL-RLC that binds nonspecifically. The functionally incorporated FDNASL-RLC, which binds very tightly, is not extracted by the extraction solution. A similar approach of including labeled RLC in the extraction solution was used previously in fluorescence studies (55,72)**.**

The spectrum from fiber bundles treated with this new exchange procedure, V_{new} (**Figure 19**, A) is different from the spectrum of bundles treated with the old procedure, V_{old} (**Figure 19**, B). Based on a qualitative inspection of the spectra in **Figure 19**, it is clear that the new procedure results in a much higher degree of orientation. We

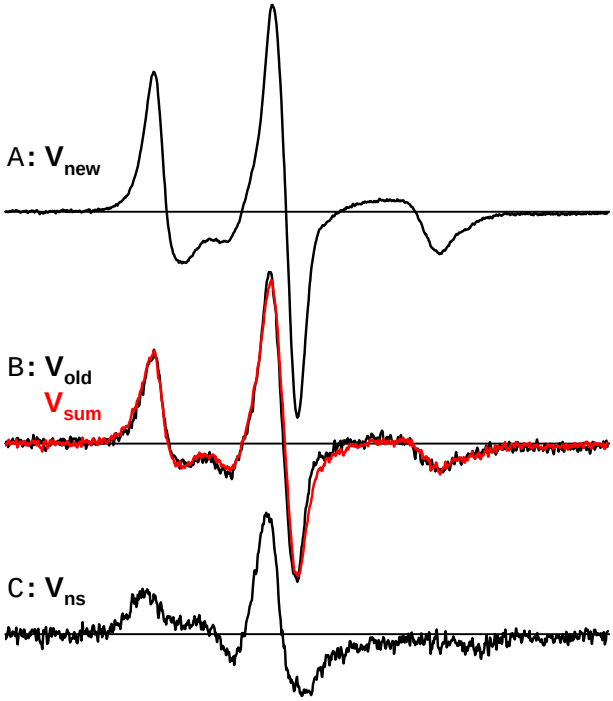

Figure 19 Improved RLC exchange.
EPR Spectra demonstrate a dramatic decrease in nonspecific RLC binding with the new RLC exchange procedure. Spectra were acquired in rigor with the fiber axis parallel to the field. A: Spectrum V_{new} from the new procedure, used in the current study. B: Spectrum V_{old} from the old procedure (54), overlaid on V_{sum} (red) that is the sum of 0.63 V_{new} + 0.37 V_{ns}. C: V_{ns} is the spectrum of nonspecifically bound spin-labeled RLC, as described in text.

hypothesize that this is due to a decrease in the fraction of nonspecifically bound RLC, which is disoriented. If this hypothesis is true, it follows that V_{old} is a linear combination of V_{ns} and V_{new}, that is, a combination of nonspecifically bound and functionally incorporated RLCs,

$$V_{old} = V_{sum} = x_{ns}V_{ns} + (1-x_{ns})V_{new}$$

where x_{ns} = mole fraction of nonspecifically bound RLCs. Assuming this model, the best fit was obtained with $x_{ns} = 0.37$. The fit assuming this model is quite good (**Figure 19**, B) indicating that V_{old} is at least 37% V_{ns} (nonspecific RLC). Simulation of minced spectra (see EPR spectroscopy) indicates that V_{new} still contains a small amount (< 15%) of V_{ns}. This demonstrates that V_{old} is actually 52% V_{ns}, consistent with previous measurements (20), and the new exchange protocol (procedure below) reduces this to less than 15%.

Section 3: Method for RLC-exchange

Rabbit psoas fiber bundles were dissected from glycerinated strips into bundles measuring 0.3-0.5mm in diameter and 3–5 cm in length. Dissected bundles were then tied with silk thread at each end, and pulled into a glass capillary (25 μL Drummond Microdispenser, Drummond Scientific, Broomall, PA). The thread, and consequently the fiber bundle, were held stationary inside the capillary by capping the end of the capillary with silicone tubing. Thus the fiber bundle was held at a fixed length throughout RLC exchange, pPDM crosslinking, and EPR. The RLC exchange procedure was adapted from a previously described method (54), and is described below in seven steps. The 200 μL rinses were done one bundle at a time using a pipet to inject solution through the capillary, otherwise a peristaltic pump (flow rate 0.5 mL/min) was used to perfuse the fiber bundles. Capillaries were connected in series when performing an RLC exchange on more than one fiber bundle.

1. Wash with pre-extraction solution (20 mM Imidazole, 20 mM KCl, 10 mM EDTA, 10 mM *trans*-1,2-Diaminocyclohexane-*N,N,N′,N′*-tetraacetic acid monohydrate (CDTA), 2 mM EGTA, pH 7.0), 10 min at 4^{o}C.
2. Circulate ≥ 310 μL of extraction solution (pre-extraction solution with 10 mM 5, 5′- dithiobis (2-nitrobenzoic acid)(DTNB)) with FDNASL-RLC (≥ 0.6 mg/ml) over each fiber bundle, 10 min at 23^{o}C.
3. Rinse three times with 200 μL of rigor solution 130 (RS130) (130 mM KPr, 2 mM $MgCl_2$, 1 mM EGTA, 20 mM MOPS, pH 7.0).
4. Incubate in RS130 (pH 8.0) with 30 mM DTT, 1.5 hours at 4^{o}C.

5. Wash with RS130, 10 min at 4°C.
6. Incubate with 40 μL of RS130 + 5 mM MgATP + 4 mg/mL TnC, 1 hour at 4°C. After 1hr, add an additional 40 μL of TnC solution, and incubate for another hour at 4°C.
7. Rinse three times with 200 μL of RS130.

If the exchanged fiber bundles were not used immediately after exchange, they were placed in storage solution and stored at -20°C.

Section 4: SDS-PAGE

The extent of RLC extraction and reconstitution was determined by densitometric analysis of SDS-PAGE on fiber homogenates. Fiber homogenates were prepared by mechanically homogenizing muscle fibers with a PowerGen Model 125 homogenizer (Fisher Scientific, Pittsburgh, PA). Three fiber bundles (0.3-0.5mm in diameter and 3–5 cm in length) were homogenized in 375 μL of RS130 for 12 minutes using 15 s pulses alternating with 15 s pauses. After homogenization, 12 μg of fiber homogenate was loaded into an 18% Tris-HCl gel (Bio-Rad Laboratories). The gel was run at 200 V for 75 minutes. This is a longer run time than recommended by Bio-Rad, but we found that the lengthened run time improved separation between the RLC and TnC bands. Under these conditions endogenous RLC, FDNASL-RLC, TnC, ELC1, and ELC2 bands are well resolved (**Figure 20**), making it possible to determine the relative amount of each protein. The extent of RLC extraction and reconstitution was calculated by comparing the ratio of the intensities of the endogenous RLC and FDNASL-RLC bands from the exchanged

fiber homogenate (**Figure 20**, lane 4) with the intensities from the control fiber homogenate (**Figure 20**, lane 3). RLC intensities were normalized by the intensity of the ELC1 and ELC2 bands, as described previously (54,73). Since TnC is also extracted during the RLC exchange process, TnC was reconstituted after extraction. The extent of TnC reconstitution was determined using the same method used for the RLC. Densitometric analysis indicates that 54 ± 10 % of the endogenous RLC was extracted. After reconstitution with FDNASL-RLC, the total RLC content was restored to 92 ± 3% relative to control values. TnC extracted during the exchange procedure was completely replaced.

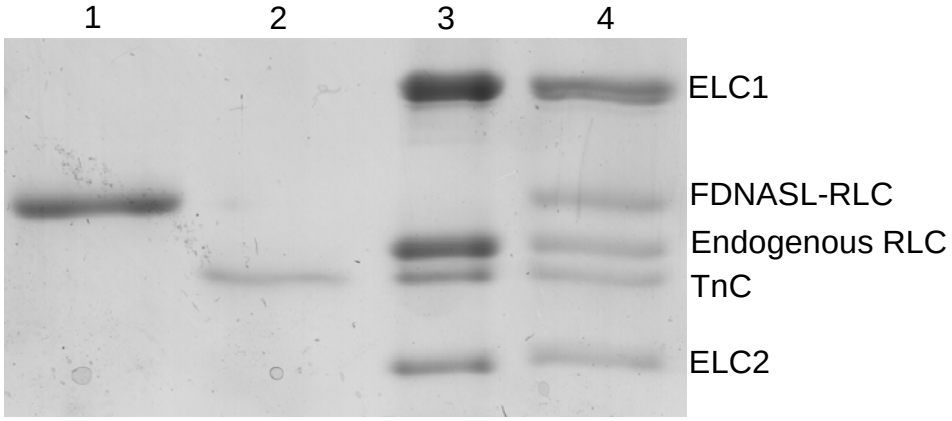

Figure 20 Extent of RLC exchange.
18% polyacrylamide gel showing protein composition of control and extracted fiber homogenates. Lanes: (1) FDNASL-RLC, (2) purified rabbit skeletal TnC, (3) control muscle fiber homogenate, (4) exchanged muscle fiber homogenate.

Section 5: ATPase assays

Muscle fiber function after RLC exchange was assessed by measuring the Ca dependence of myofibrillar MgATPase activity, as measured with an NADH-enzyme linked microtiter plate assay (200 μL per well) in which the rate of oxidation of NADH is linked

to the rate of ATP hydrolysis (74,75). Each well contained 50mM MOPS, 0.1 M KCl, 5mM $MgCl_2$, 1mM EGTA, 0.5 M phosphoenolpyruvate, 2.5 mM ATP, 0.2 mM NADH, 1 IU of pyruvate kinase, and 1 IU of lactate dehydrogenase. Myofibrils were prepared as described above (SDS-PAGE), except that the homogenization solution was 60mM KPr, 1 mM EGTA, 1 mM NaN_3, 25 mM MOPS, pH 7.0. The protein concentration was adjusted to 2mg/mL and combined (1:1 by volume) with sucrose solution (2 mM NaN_3, 0.6 M sucrose, 40mM MOPS, pH 7.0), and 10 μL of myofibril/sucrose solution was added to each well. The oxidation of NADH was followed by measuring the rate of decrease in absorption at 340 nm with a SpectraMax Plus 384 microplate reader (Molecular Devices). [Ca^{2+}] was controlled by EGTA buffering (76). The results were fitted with the Hill equation:

$$V = V_{max}/[1 + 10^{-n(pKCa - pCa)}] \qquad \text{eq. 3.1}$$

where *V* is the ATPase rate and *n* is the Hill coefficient. Control fiber bundles underwent a mock exchange, in which the extraction and reconstitution steps were replaced with RS130 washes in order to mimic the exchange procedure without extracting or reconstituting any protein.

To assess the modification of SH1 and SH2, the K/EDTA and Ca/K ATPase activities of myofibrils were measured at high ionic strength by measuring phosphate liberation after acid quench (77). The incubation solution (25°C) contained 0.6M KCl, 50 mM MOPS, and 10 mM of either EDTA (K/EDTA ATPase) or $CaCl_2$ (Ca/K ATPase) (pH 7.5). Myofibrils were prepared using the same method as described above (SDS-PAGE), except the fibers were homogenized in a solution of 10 mM MOPS. Using a

previously described method (5), the fraction of crosslinked heads was calculated using the K/EDTA and Ca/K ATPase activities from control and crosslinked fibers.

Figure 21

Simulations (**Figure 21**) illustrate the dependence of EPR spectra on θ′ when the fiber axis is aligned parallel (red, θ′ = θ) and perpendicular (blue, where θ′ exhibits more disorder due to helical symmetry of the muscle fiber) to H (5).

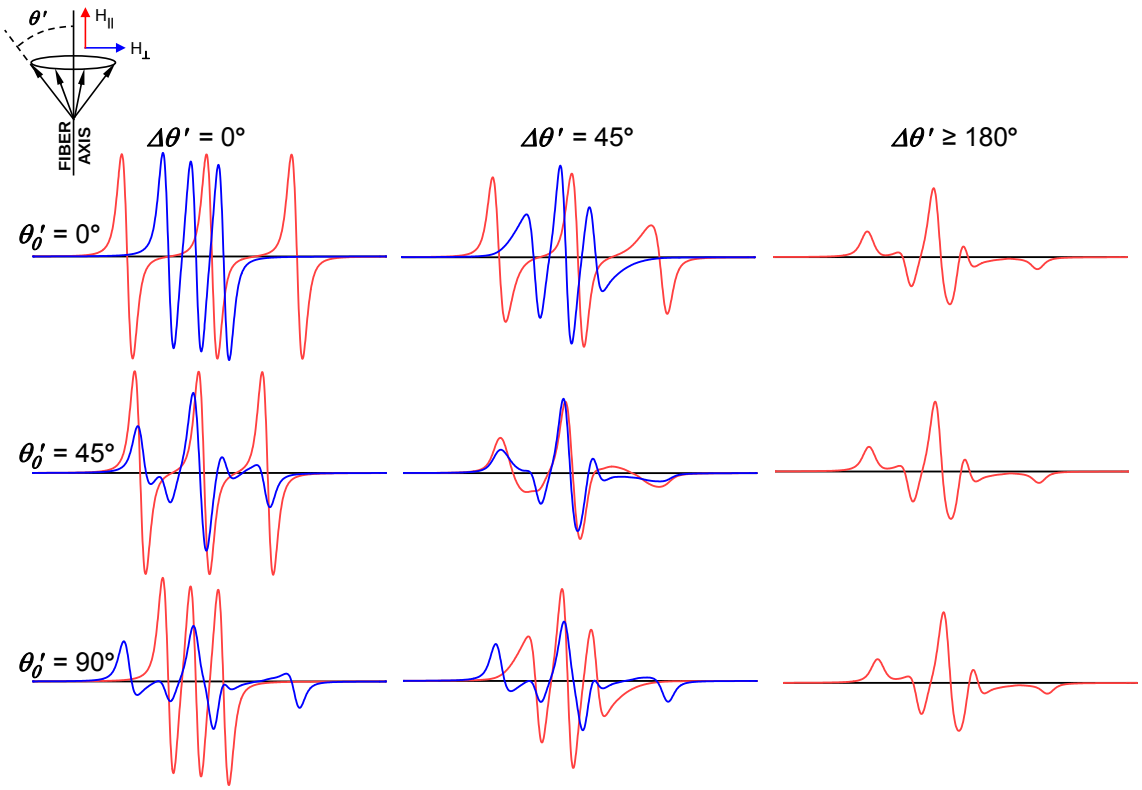

Figure 21 Sensitivity of conventional EPR to orientational distributions.
Simulated EPR spectra show the dependence of conventional EPR (V_1) on tilt angle θ′ of the spin label principal axis relative to the muscle fiber axis. A Gaussian distribution of θ′ is assumed, where θ_0' is the center of the distribution and Δθ′ is the full width at half-maximum. Spectra correspond to the muscle fiber axis oriented parallel (red) and perpendicular (blue) to the applied magnetic field (H). The difference between red and blue provides a clear indication of the degree to which the protein is oriented relative to the muscle fiber axis. In the right column, corresponding to complete disorder, there is no difference between red and blue, so blue is not visible.

Figure 22

In addition to being sensitive to orientation, EPR is sensitive to rotational dynamics on the timescale of picoseconds to microseconds (53).

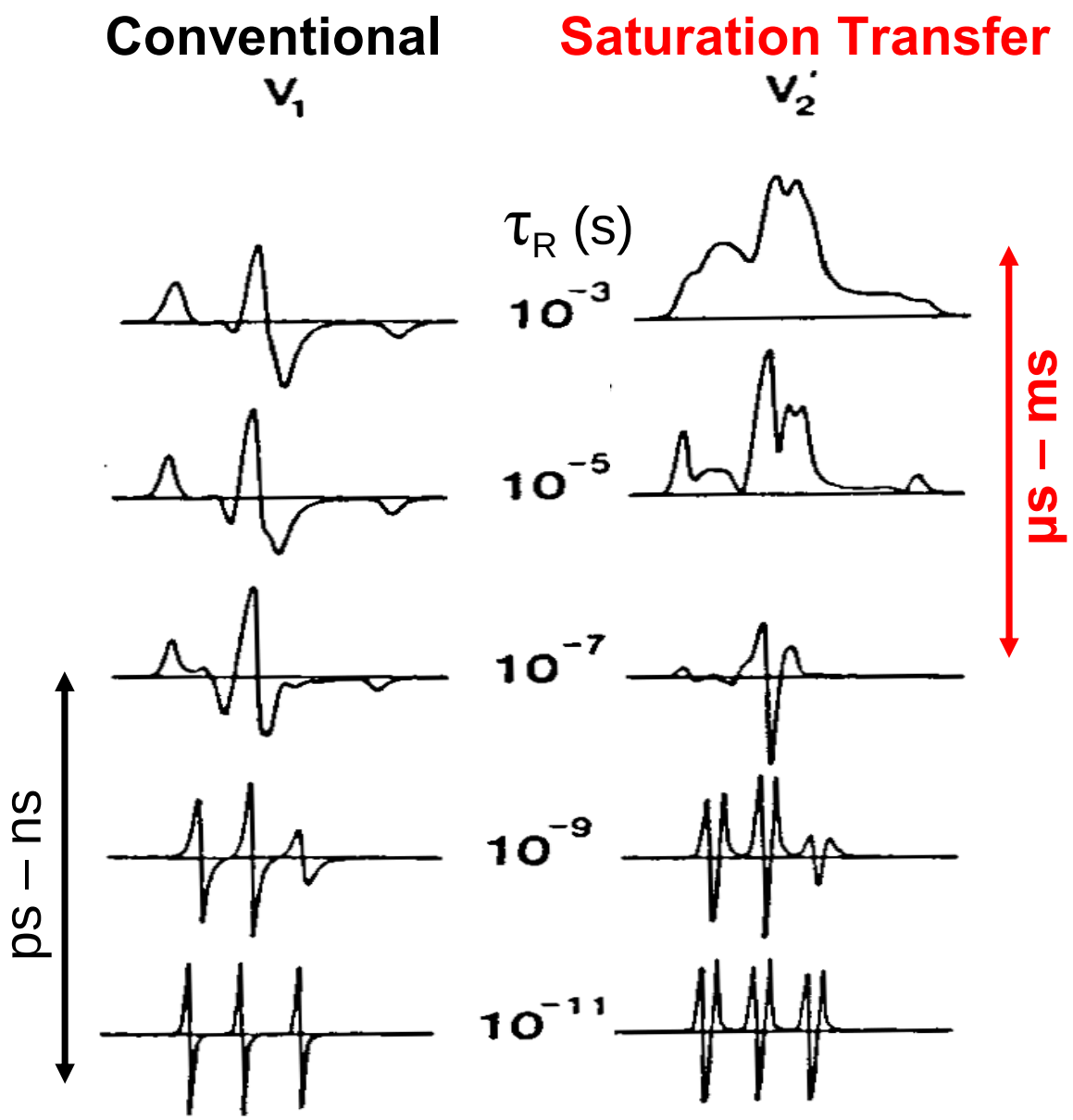

Figure 22 Dependence of EPR spectra on isotropic rotational correlation time. Sensitivity of conventional (V_1, left) and saturation transfer (V_2', right) EPR spectra to rotational dynamics of nitroxide spin labels. V_1 spectra are sensitive only to submicrosecond rotational correlations times (τ_R), while V_2' spectra are sensitive to much slower motions. Adapted from (5).

3.7 Future Directions

The work presented in chapter three will be expanded, on at least two fronts: (i) the implementation of an improved spin-labeling method and (ii) the use of other small molecules that perturb myosin function. This section briefly summarizes preliminary results and the future of this work.

The driving force for an improved spin-labeling technique is to reduce probe motion and increase the resolution of EPR for making structural measurements. In this work, spin labels are used as reporters of protein structural dynamics. So ideally, a spin label would be rigidly coupled to the protein backbone. However, in practice, probe flexibility can lead to a loose coupling between the spin label and the protein. One approach to decreasing spin label flexibility is to use a bifunctional spin label (BSL) (See Chapter 4 for more on BSL). Traditional spin labels (such as the FDNASL used in Chapter 3) attach monofunctionally to a single Cys residue, while BSL attaches bifunctionally at residue positions *i* and *i*+4 on an α-helix. The rational for using BSL is that the bifunctional attachment will limit probe flexibility compared to a monofunctional spin label. In Chapter 3 of this work, FDNASL was used to label the RLC at residue 108. FDNASL at this residue is moderately immobilized. However, spectra of minced fiber bundles, labeled with either FDNASL or BSL, demonstrate that FDNASL is more mobile than BSL, as indicated by the narrower splitting of the FDNASL spectrum (**Figure 23**).

Assuming that the spin labels are undergoing rapid (τ_r < 0.1 ns) restricted rotational motion, the amplitude of the motion can be described by the order parameter S.

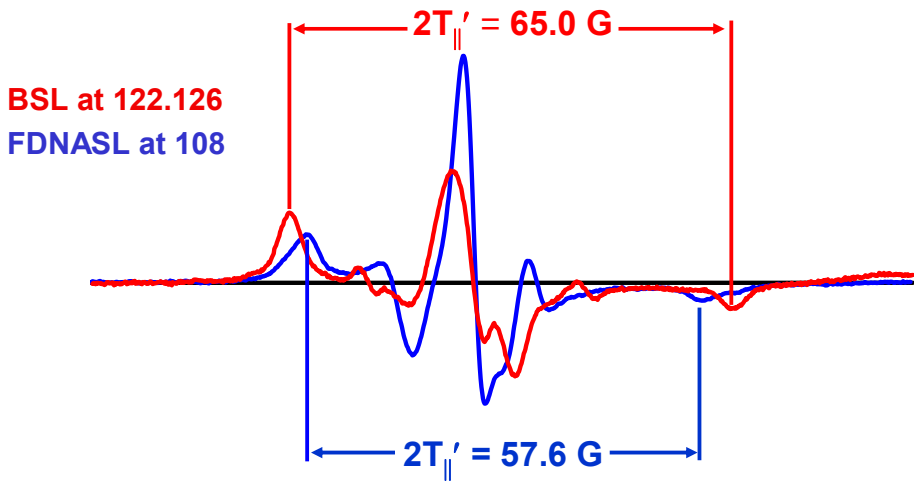

Figure 23 FDNASL vs. BSL on the RLC in psoas fibers.
Fiber bundles were labeled with FDNASL at residue 108 (blue) or BSL at residues 122.126 (red). Fiber bundles were minced and spread on a flat cell. The flat cell was placed inside the TE_{102} cavity with the face of the flat cell oriented perpendicular to the external magnetic field H. The splitting $2T_{\parallel}'$ was used to calculate the order parameter S.

In general

$$S = (\text{observed anisotropy})/(\text{maximum anisotropy})$$

For a highly ordered system (rigid limit) S = 1, and for completely isotropic motion S = 0 (18). The order parameter is related to the angular amplitude of the motion, described by the angle θ (18).

$$S = \tfrac{1}{2} (3 \langle \cos^2 \Delta\theta \rangle - 1)$$

Where ⟨ ⟩ indicates the time-averaged angular displacement. The order parameters for BSL and FDNASL can be determined from the minced fiber spectra (**Figure 23)** using the following expression:

$$S = (T_{\parallel}' - T_0)/(T_{\parallel} - T_0) \qquad \text{eq. 3.2}$$

where $T_{\parallel}$ is ½ the rigid-limit splitting between the outer peaks (let $T_{\parallel}$ = 35 G), $T_{\parallel}'$ is the splitting measured from the experimental spectra (**Figure 23**), and T_0 is the splitting at the isotropic limit (let T_0 = 16.3 G). If the motion of the spin label is assumed to be restricted

to a cone with a cone angle of θ_c (**Figure 24**), then S can be used to infer the amplitude of the motion within the cone (i.e. θ_c).

$$S = \tfrac{1}{2}(\cos\theta_c + \cos^2\theta_c) \qquad \text{eq. 3.3}$$

Using these assumptions and the splitting determined from the spectra in **Figure 23**: S_{BSL} = 0.87 with $\theta_{c,BSL}$ = 24° and S_{FDNASL} = 0.66 with $\theta_{c,FDNASL}$ = 41°. These results demonstrate that BSL's rapid motion is significantly more restricted than FDNASL.

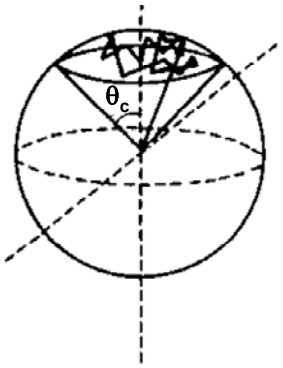

Figure 24 Wobble in a cone.
Model for random motion of a spin label within a cone. The amplitude of the motion is defined by the cone angle θ_c. Adapted from (18).

The mobility of FDNASL does not trivialize the results discussed previously in this chapter. As seen in **Figure 14** and **Figure 16**, the observed changes are dramatic. The change in θ_0' between states is at least 13° and the change in the rotation dynamics of the RLC (described by τ_R) is several orders of magnitude; meaning that a higher resolution technique would not change the conclusions made in section 3.5. However, greater resolution would make it possible to make more precise conclusions. For example, when simulating FDNASL spectra it was not possible to determine with certainty if the

oriented spectra were best fit assuming one or two orientational distributions of the RLC. Therefore, the results of spectral fitting are presented as the average orientational distribution for each state (described by θ_0' and $\Delta\theta'$). Since the bifunctional attachment of BSL rescricts the amplitude of probe motion, it may provide the resolution needed to discern between these two models. However, the BSL results (**Figure 23)** are preliminary. The development of this technology and knowledge is the topic of Chapter 4, and the BSL-RLC project will need to be revisited after this technique is fully understood.

As mentioned above, another way in which this work will be continued is the use of other small molecules that perturb myosin function. In this work, pPDM was used to trap the elusive A.M′.D.P complex. Another molecule of interest is blebbistatin (**Figure 25**, A). Blebbistatin is a selective inhibitor of myosin 2 that inhibits motor activity and ATPase, and binds deep within the actin binding cleft on the myosin CD (66) (**Figure 25**, B). Blebbistatin binds preferentially to the ATPase intermediate with ADP and P_i bound, and it inhibits P_i release (78). Another study found that myosin complexed with ADP and blebbistatin adopts a primed lever arm position and maintains the strong actin binding properties of the myosin ADP complex (41). Collectively, these results indicate that myosin complexed with blebbistatin and ADP is analogous to a state populated at the beginning of force generation; a post-hydrolysis pre-P_i-release state that binds actin and has a LCD confirmation primed to complete the power stroke. This complex of myosin with ADP and blebbistatin provides another useful tool for studying the initial force-generating states that are short lived, and therefore difficult to study, but essential in the

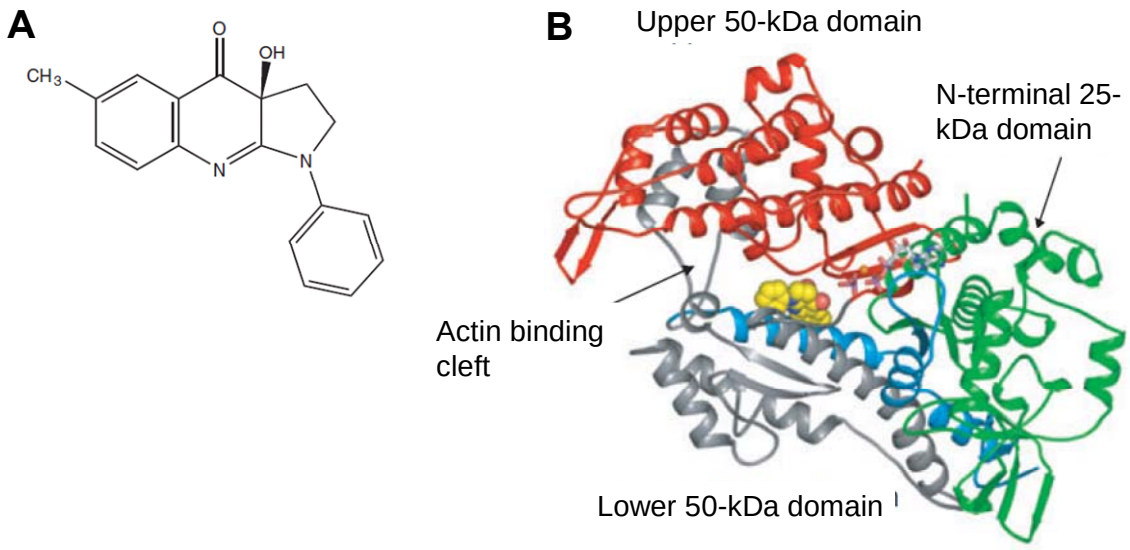

Figure 25 Blebbistatin
A: Chemical structure of the myosin inhibitor blebbistatin. B: Structure of *Dictyostelium discoideum* myosin II with blebbistatin (yellow) bound in the actin binding cleft. Adapted from (66).

molecular mechanism of force generation. Coupled with the use of BSL, the future of this work is exciting, specifically for elucidating the role of the LCD. Does the LCD act as a semirigid rod to amplify the force producing rotation of the CD (7,10), or does it simply follow the CD through it force-producing transitions? Additionally, as mentioned above, an important challenge for the future is to test the models derived from these "trapped" states (**Figure. 18)** by observing the proposed states not by trapping, but by resolving them in the transient phase of a structural kinetics experiment (67).

Chapter 4: A High-resolution EPR Technique for Measuring Protein Structural Dynamics

4.1 Overview

We present a high-resolution method for measuring protein structural dynamics using site-directed spin labeling (SDSL) with a bifunctional spin label (BSL) and electron paramagnetic resonance (EPR) spectroscopy. The use of BSL is a key feature of this work. BSL attaches at residue positions *i* and *i*+4 on an α-helix, which drastically reduces probe motion compared to monofunctional labels. Measurements were also made with the monofunctional spin label MSL for comparison. Two complimentary EPR techniques were used: (i) conventional EPR to measure dynamics and orientation and (ii) dipolar electron-electron resonance (DEER) to measure distance distributions between pairs of spin labels. *Dictyostelium discoideum* myosin II was used to exemplify these techniques, and spin labels were introduced to measure structural dynamics of the relay helix (a key helix dynamically involved in myosin motor function). Measurements were made in apo and ADP biochemical states. Conventional EPR spectra of BSL reveal that (i) BSL is strongly immobilized on myosin, (ii) there are two structural states of the relay helix and (iii) ADP has influences the orientational distributions of these structural states. MSL spectra indicate that MSL is flexible on myosin and provide no clear resolution of orientational distributions in apo or ADP biochemical states. Similarly, DEER waveforms

from BSL reveal two distance distributions in both apo and ADP states, while MSL reveals only one. In all cases, BSL spectra and DEER waveforms reveal structural information that is masked by the nanosecond motions of MSL.

4.2 Introduction

Electron paramagnetic resonance (EPR) spectroscopy coupled with spin labeling has been a useful tool in structural biology and biophysics (79). This approach has been used to measure protein orientation, dynamics, and intraprotein distances (7). In some instances, labeling conditions can be optimized such that a cysteine specific spin label (see Section 2.4) will selectively label a native cysteine or cysteines (29,80-82). In other cases, protein mutagenesis is used to replace all reactive cysteines with a similar amino acid (such as alanine) and engineer a cysteine at the desired labeling site. The EPR spectrum of the spin label, covalently attached to the desired cysteine residue, can then be used to characterize protein orientation (20,29), dynamics (82,83), and in the case of two labeling sites, intraprotein distances (21). This technique is referred to as site-directed spin labeling (SDSL), and it has proved to be very useful. However, the resolution of this approach is limited by the flexibility of the spin label. Traditional spin labels attach monofunctionally (i.e. one bond is made between the spin label and the protein backbone), and flexibility about this bond can complicate analysis and limit spatial resolution. This limitation is evident in Chapter 3 and the work by Baker et al. (20), in which FDNASL is attached at Cys108 on the regulatory light chain (RLC) in rabbit psoas muscle. FDNASL at Cys108 on the RLC is relatively immobile, but not completely

immobilized (FDNASL has some restricted nanosecond motion, see Section 3.7). This nanosecond motion does not limit the ability to detect large changes in orientation and dynamics, such as observed in **Figure 14** and **Figure 16**. However, it does limit the ability to resolve smaller changes, such as those expected of the RLC during muscle contraction.

In an effort to evade the limitations imposed by probe flexibility, some groups have began using a bifunctional spin label (BSL) (5,84,85). BSL attaches bifunctionally, two bonds are made, at residues i and i+3 or i and i+4 on an α-helix and i and i+2 on a β-sheet (85). The rational for using BSL is that the bifunctional attachment will limit probe motion, simplifying analysis and increasing the resolution of EPR for measuring protein structural dynamics. In 2008, Thompson et al. utilized the crosslinking capability of BSL to simultaneously spin-label myosin and trap it in a post-hydrolysis state in the early stages of force generation. EPR spectra demonstrate that BSL was rigidly attached to myosin, the myosin head was orientationally disordered on actin, and myosin dynamics were slow (on the millisecond timescale) (5). Another study used BSL to measure tropomyosin dynamics. BSL spectra revealed variations in the rates of motion along the length of tropomyosin (84). A third study used EPR and x-ray crystallography of BSL labeled T4 lysozyme and intestinal fatty acid-binding protein to demonstrate that BSL attaches to an α-helix in a single well-ordered confirmation (85).

EPR spectra from the BSL results discussed above (5,84,85) demonstrate that BSL is rigidly coupled to the protein backbone, and this immobilization simplifies the analysis and increases the resolution of EPR for measuring intraprotein distances and

protein dynamics compared to monofunctional spin labels. However, there has yet to be a BSL-EPR study in which BSL is utilized to measure the orientational distribution of an oriented system. In the BSL-S1 work (5) EPR spectra of BSL were used to determine the orientational distribution of myosin subfragment 1 (S1) on actin. Under certain conditions myosin is well oriented on the actin filament, but in the BSL-S1 work BSL was used to crosslink Cys707 to Cys697 on the catalytic domain (CD) of S1, effectively trapping myosin in a highly disordered state. In the other two studies (84,85), EPR of BSL was used to measure intraprotein distances and protein dynamics, but not orientational distributions.

One emphasis of the current work is to describe the methodology for making all three measurements (dynamics, orientation and distances), and demonstrate qualitatively the advantage of using BSL over the monofunctional spin label (MSL). *Dictyostelium discoideum* myosin II was selected as the model system for which to test this approach. *Dictyostelium discoideum* is a amoeba that often lives in soil, and is commonly referred to as slime mold. There is a strong background in genetically modifying *Dictyostelium* myosin (1), making it an attractive option for engineering labeling sites at desired locations. Additionally, it has been shown that the force generating region of *Dictyostelium* myosin is similar in structure to muscle myosin (64). In this work, we have measured nucleotide dependent structural transitions of myosin's force generating region.

The Dicty myosin background used for introducing labeling sites was a Cys-lite version of the motor domain, referred to as S1dC. S1dC was labeled on the relay helix, a helix in the CD that undergoes structural transitions that are essential for motor function

(21,67,86). S1dC was labeled with BSL at residues 494.498 on the relay helix and at 639.643 on an adjacent stable helix. In order to provide a monofunctional comparison, S1dC was labeled at 498 with MSL for orientational studies (**Figure 26**). Spin-labeled S1dC was then bound to actin in oriented fiber bundles and conventional EPR was used to measure BSL dynamics and relay helix orientation. DEER was used to measure the distance distribution between these two labeling sites for S1dC in solution. All measurements were done in apo and ADP biochemical states.

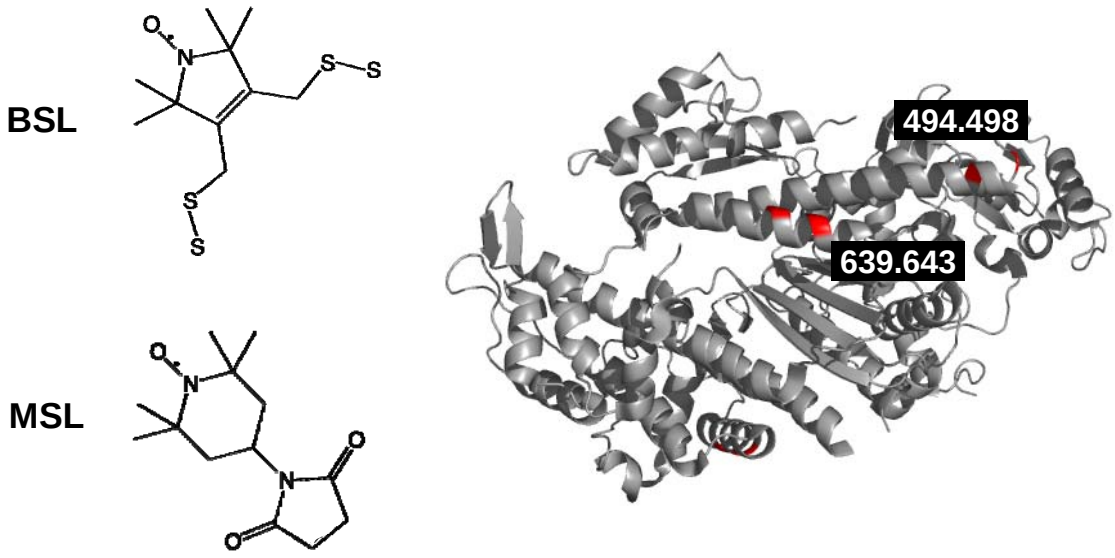

Figure 26 BSL, MSL and Dictyostelium *discoideum* myosin II catalytic domain.
Left: The two spin labels used in this work, BSL and MSL. Right: Crystal structure (1FMV) highlighting the labeling sites (red residues).

4.3 Methods

Muscle fiber preparation

Glycerinated rabbit psoas muscle fiber bundles were prepared and stored in a storage solution containing 1:1 mixture of rigor solution (60 mM KPr, 2 mM $MgCl_2$, 1 mM EGTA, 25 mM MOPS, pH 7.0, 25^o C) and glycerol at -20^{o}C for up to 6 months without significant loss of function (47).

Myosin preparation

Mutants of *Dictyostelium discoideum* myosin II were constructed and purified as described previously (21,87). The base construct used was a Cys-lite mutant of the myosin CD (gift from James Spudich) that contained no reactive Cys residues (88). This construct was truncated at amino acid 758, and is referred to as S1dC. Myosin mutants were made for conventional EPR and DEER. Two Conventional EPR mutants were made with BSL labeling sites: one site was on the C-terminus of the relay helix at Y494C.K498C and the other at A639C.A643C on an adjacent helix. Two conventional EPR mutants were also made for monofunctional labeling, K498C and A639C. For DEER, one mutant was made that contained two BSL labeling sites, Y494C.K498C and A639C.A643C. These proteins were constructed and prepared by Sarah E. Blakely, Evan A. Smith, and Rebecca J. Moen.

Spin-labeling

S1dC was spin-labeled for two types of EPR experiments, conventional EPR and DEER. For conventional EPR (one labeling site per S1dC) di-Cys S1dC mutants were spin-labeled with BSL (3,4-bis-(methanethiosulfonyl-methyl)-2,2,5,5-tetramethyl-2,5-dihydro-1h-pyrrol-1-yloxy) and mono-Cys mutants were labeled with MSL (N-(1-oxy-2,2,6,6-tetramethyl-4-piperidinyl)maleimide). S1dC was dissolved in labeling solution (20 mM MOPS, 50 mM KCl, 3 mM $MgCl_2$, 1 mM EDTA, pH 7.5), and treated with 5 mM DTT for 1.5 hrs. DTT was removed using two Zeba spin columns (Thermo Fisher Scientific Inc., Rockford, IL) equilibrated with labeling solution. The protein concentration was then adjusted to 100 μM, and BSL was added at 200 μM and the sample was incubated for 1 hr on ice. Unreacted BSL was removed with a spin column equilibrated with EPR solution. The method for MSL labeling was the same as BSL labeling, except 500 μM MSL was added to 100 μM S1dC, and the incubation time was 12 hrs (or over night). After labeling, the S1dC concentration was adjusted to 100 μM, and bound to actin in oriented fiber bundles (described below). DEER samples contained two di-Cys labeling sites, and were labeled using the same method as described above with the following exception: S1dC (100 μM) was incubated with 400 μM BSL during labeling (single di-Cys mutants for conventional EPR were labeled with 200 μM BSL).

Decorating muscle fiber bundles with spin-labeled S1dC

When measuring dynamics and orientational (conventional EPR), S1dC was bound to the actin filament in rabbit psoas fiber bundles. These fiber bundles with S1dC bound are

referred to as decorated fibers. The first step in decorating fiber bundles was to dissect an EPR size fiber bundle from the glycerinated muscle fiber strips in storage solution. The glycerinated fiber strips were dissected into bundles measuring 0.3-0.5mm in diameter and 3–5 cm in length. Dissected bundles were then tied with silk thread at each end, and pulled into a glass capillary (25 μL Drummond Microdispenser, Drummond Scientific, Broomall, PA). The thread, and consequently the fiber bundle, were held stationary inside the capillary by capping the end of the capillary with silicone tubing. Spin-labeled S1dC was then bound to the fiber bundle as follows. (i) Spin-labeled S1dC was put into a low-salt EPR solution (40 mM MOPS, 1 mM EGTA, 2 mM $MgCl_2$, 15 mM KPr, pH 7.0) and the S1dC concentration was adjusted to ~ 100 μM. (ii) 80 μL of 100 μM S1dC was injected into the glass capillary containing the fiber bundle. The ends of the capillary were sealed with parafilm (Pechiney Plastic Packaging Company, Chicago, IL). (iii) The fiber bundle was incubated with S1dC for one hour on ice. (iv) After one hour, the fiber bundle was connected to a peristaltic pump using the silicone tubing, and free S1dC was washed away. At this point the fiber bundle, still connected to the peristaltic pump, was placed inside an EPR cavity equilibrated at 4^{o} C.

Conventional EPR spectroscopy

Conventional EPR experiments were performed using a similar method as described in section 3.3. Spectra were recorded at X-band (9.5 GHz) with a Bruker (Billerica, MA) E500 spectrometer, using either a TE_{102} (Bruker 4104OR-R) or TM_{110} (Bruker 4103TMA) cavity. The sample temperature was maintained at 4^{o}C by flowing

temperature-controlled N_2 gas through a nozzle attached to the optical port on the front of the cavity (TE_{102}) or a quartz dewar inserted into the bottom of the cavity (TM_{110}). Maintaining the temperature at 4^oC is important for BSL experiments due to the reversibility of the labeling reaction and the observation that the rate for BSL detaching from the protein is slower at 4^oC than at ambient temperatures. The sweep width was 120 G (1024 points), sweep time was typically 41.94 s (conversion time 40.96 ms), and the center field value H_C was set proportionally to the microwave frequency ν ($H_C = \nu/2.803$ MHz/G, corresponding to a g value of 2.0027, the value of g_z for a typical nitroxide) so that all spectra were equivalently aligned. The Microwave power was set from 20 mW to 32 mW, to maximize the signal intensity without causing significant saturation. The modulation frequency was 100 kHz (first harmonic), and the peak-to-peak modulation amplitude was 2 G. The filter time constant was set equal to the conversion time (40.96 ms).

Conventional EPR spectra (V_1) of oriented fiber bundles were acquired with the long axis of the fiber bundle oriented either parallel (using a modified TM_{110} cavity (20)) or perpendicular (using a TE_{102} cavity) to the applied magnetic field H_0. The fiber bundle was connected to a peristaltic pump (as described above) and perfused with solution at a rate of 115 μL/min. Perfusion served the purpose of removing any free BSL and making it possible to readily change the biochemical state by changing the perfusion solution. EPR spectra were acquired in either EPR solution (40 mM MOPS, 1 mM EGTA, 2 mM $MgCl_2$, 15 mM KPr, pH 7.0) or ADP solution (40 mM MOPS, 1 mM EGTA, 2 mM $MgCl_2$, 5 mM MgADP, pH 7.0). For EPR experiments on randomized samples, fibers in

EPR solution were minced with a razor blade and placed in a quartz flat cell that contained a well of dimensions 0.5 x 1.0 x 0.05 cm (WG-806-Q, Wilmad-Labglass, Buena, NJ). Excess moisture was wicked away and a coverslip was placed over the sample well and sealed with Parafilm M (Pechiney Plastic Packaging Company, Chicago, IL) to prevent sample dehydration. The flat cell assembly was centered in the TE_{102} EPR cavity with its face oriented parallel or perpendicular to H_0.

Dipolar electron-electron resonance (DEER)

DEER waveforms were acquired using the same methods as described in (21), and briefly summarized below. Waveforms were acquired with an Elexsys E580 spectrometer (Bruker Biospin) equipped with a dielectric resonator (MD-5; Bruker Biospin), using a four-pulse DEER sequence (89) with a 16-ns $\pi/2$ pulse, and a 40- to 48-ns ELDOR pulse. The pump frequency was centered on the central resonance of the nitroxide spin label, and the observe frequency was set to the low-field resonance 67 MHz away. Temperature during the acquisition was set to 65° K. Complexes of myosin with nucleotide were obtained as described (64). Myosin samples (50–75 μM) were flash-frozen in liquid nitrogen before being placed in the spectrometer. Buffer contained 20 mM EPPS, 6 mM MgCl2, 1 mM EGTA, and 10% glycerol (pH 8.0). Spin echo signals were analyzed with the DeerAnalysis software suite (90), which fits simulated DEER waveforms to the data assuming one or two Gaussian interprobe distance distributions.

$$\rho(r) = \frac{1}{\sigma\sqrt{2\pi}} \exp\left(-\frac{(r-R)^2}{2\sigma^2} \right), \qquad \sigma = \frac{FWHM}{2\sqrt{2\ln(2)}} \qquad \textbf{[eq. 4.1]}$$

Sample preparation, acquisition, and analysis was performed by Rebecca J. Moen and Zachary M. James.

4.4 Results

Spin label mobility

In this work, spin labels are used as reporters of protein orientation and dynamics. Therefore, it is advantageous to use a spin label that is rigidly coupled to the protein backbone because large amplitude motions of spin labels relative to the protein complicates spectral analysis and dramatically decreases the resolution of this approach. We have used conventional EPR to measure the order parameter (S) and cone angle (θ_c) of BSL and MSL bound to the relay helix in S1dC. The order parameter and θ_c were determined using the same model described in detail in Sections 3.7. Namely, rapid (τ_r < 0.1 ns) rotational motion restricted to a cone with cone angle θ_c (**Figure 24**).

Minced fiber spectra were acquired with BSL at 494.498 and MSL at 498 (**Figure 27)**. The splitting and shapes of these spectra indicate that BSL and MSL have very different values of S and θ_c. The splitting between the low-field and high-field peaks ($2T_{\parallel}'$) of the BSL spectrum is 71.2 G (**Figure 27**, top). The rigid limit value of $2T_{\parallel}'$ is ~ 70 G, thus we conclude that BSL is strongly immobilized on the relay helix. In contrast, the splitting of the MSL spectrum is much less than 70 G, indicating that it is weakly immobilized on the relay helix (**Figure 27**, bottom). Using equations 3.2 and 3.3, it is possible to determine S and θ_c for MSL on the relay helix: S = 0.44 and $\theta_c = 56^o$.

These results demonstrate that, on the relay helix, BSL is strongly immobilized and MSL is weakly immobilize ($\theta_c = 56^o$). The rigid immobilization of BSL compared to MSL is a obvious advantage when measuring orientation and distances, as demonstrated in the following sections.

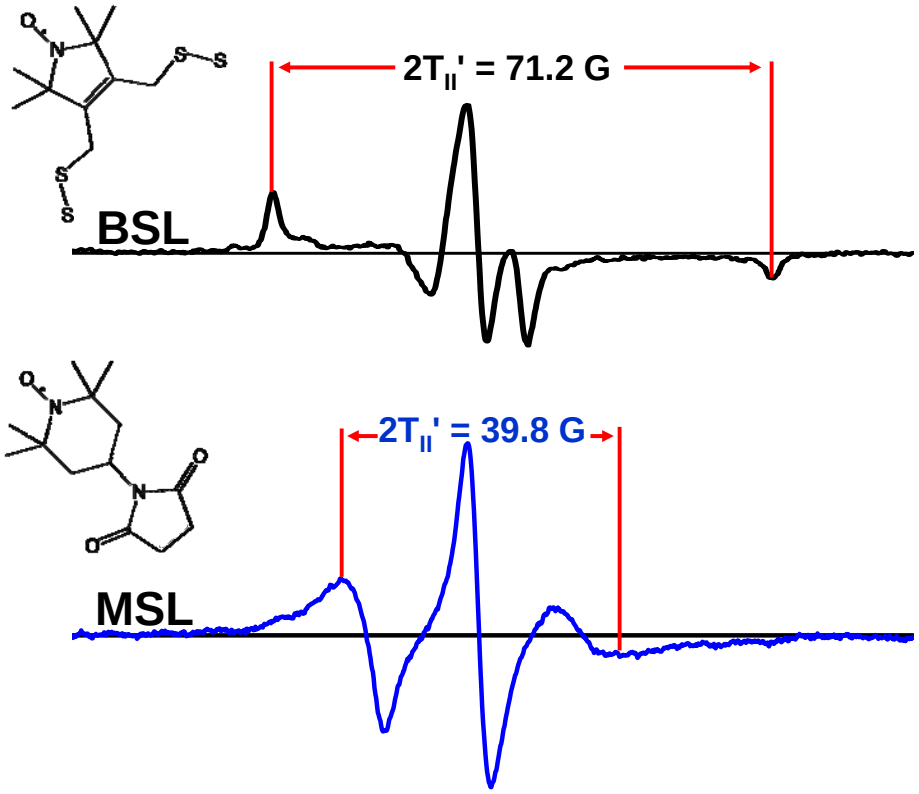

Figure 27 BSL and MSL minced spectra.
S1dC labeled with BSL (at 494.498) or MSL (at 498) was bound to actin in muscle fiber bundles. The decorated fiber bundles were minced and spread on a flat cell for acquisition. Fiber bundles were bathed in EPR solution prior to mincing. The order parameters (S) was determined from the splitting $T_{\|}'$.

Relay helix orientation measured by conventional EPR

EPR is extremely sensitive to the orientational distribution of a spin label with respect to the applied magnetic field H (see Chapter 3 and (5)). If a spin-labeled system is well

oriented, the EPR spectrum detects directly the angle θ between the spin label's principal axis and H_0 (**Figure 10**). In the case of an oriented assembly, such as a muscle fiber bundle decorated with spin-labeled S1dC, EPR can be used to measure the angle between the spin label and the assembly (actin filament) axis, θ′ (**Figure 21**). Implementing this approach, relay helix orientation with respect to the actin filament axis was measured from conventional EPR spectra of spin-labeled S1dC bound to actin in skinned muscle fiber bundles. The S1dC was labeled with MSL at 498 or BSL at 494.498, and spectra were acquired with the S1dC in apo and ADP biochemical states (**Figure 28**). Apo spectra were acquired while perfusing the fiber bundle with EPR solution, and ADP spectra were acquired while perfusing ADP solution. The MSL spectra are nearly identical in apo and ADP states (**Figure 28**, top), whereas the BSL spectra demonstrate a marked ADP effect on the relay helix (**Figure 28**, middle). This result is not surprising based on the fact that MSL is weakly immobilized on the relay helix and BSL is strongly immobilized , as determined from the minced spectra (**Figure 27**).

Given that BSL is strongly immobilized, it is possible to fit the oriented BSL spectra without having to include nanosecond probe motions in the simulation, which greatly simplifies the simulation. Additionally, the results of the fit describe the orientational distribution of the relay helix. In contrast, the MSL spectra would be very difficult to fit as the simulations would have to account for both nanosecond probe motions and protein orientation. At the time of this writing, the fitting of BSL spectra is in progress. However, even without the results of the fits it is possible to make some

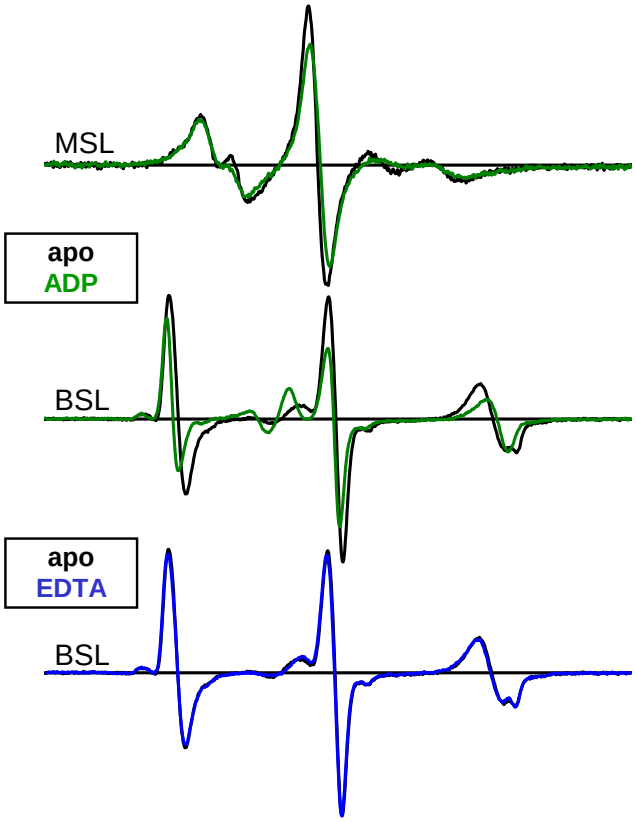

Figure 28 BSL and MSL oriented spectra.
Conventional EPR spectra of oriented fiber bundles decorated with spin-labeled S1dC. Spectra were acquired with the fiber bundles oriented parallel to H. Top: S1dC labeled with MSL at 498. Apo spectrum is black and ADP is green. Middle: S1dC labeled with BSL at 494.498. Apo spectrum is black and ADP is green. Bottom: S1dC labeled with BSL at 494.498. Black is the same apo spectrum as shown in the middle, and the blue spectrum was acquired while perfusing the fiber bundle with EDTA solution after ADP treatment, demonstrating the reversibility of the ADP effect.

conclusions about the orientational distribution of the relay helix and the effect of ADP on the relay helix. In both states, apo and ADP, the spectra contain two components, indicating two orientational distribution of the relay helix. The most distinct component has a wide splitting and sharp lines. The narrow lines are not from motional narrowing, hence they indicate a high degree of orientational order. The splitting of this component changes by 1.9 G from rigor to ADP, indicating a roughly 4^{o} rotation of the relay helix. The second lesser component also appears to change as a function of nucleotide. In the apo spectrum, this component appears less intense than it does in the ADP spectrum,

indicating that ADP increases the mole fraction of this component. Spectral fitting will make it possible to confirm or modify these conclusions and determine numerical values for the mole fraction of each spectral component and the orientational distribution. Given the mobility of MSL and the similarity between apo and ADP spectra, it was not possible to make these conclusions from the MSL spectra.

Distance distributions measured by DEER

Dipolar electron-electron resonance (DEER) is a pulsed EPR technique used to measure distances between a pair of electron spins (91). This technique uses a spin echo pulse sequence and different frequencies to selectively excite each electron. DEER waveforms are sensitive to the strength of the dipolar interaction between the electron spins, and the distance distribution is inferred from this coupling strength. Due to the dipolar interaction being proportional to r^{-3} (where r is the interspin distance) and time-resolved detection, DEER waveforms report spin-spin distances with high resolution in the range of 2 to 6 nm (21,92). In this work, DEER was used to measure the distance distribution between BSL at 494.498 on the relay helix and 639.643 on a stable helix near the relay helix. DEER waveforms were acquired with spin-labeled myosin trapped in apo and ADP biochemical states, then simulated assuming a one- or two-Gaussian interprobe distance distribution (as described in 4.3 Methods). We then compared these DEER results to previously published data from S1dC samples labeled with MSL at 498 and 639 (21).

These waveforms from MSL and BSL and the corresponding distance distributions (**Figure 29**) demonstrate the advantage of using BSL over the monofunctional spin label MSL. In both apo and ADP states, the BSL waveforms are best fit to a two-Gaussian distribution while the MSL waveforms are best fit to one (**Table 2**). In both cases, BSL and MSL, there is no significant difference between the distance distributions in apo and ADP biochemical states. However, it is worth noting that one of the distributions determined from the BSL waveform has a significantly narrower distribution (FWHM) than the MSL distribution, while the other BSL distribution is more disordered. The extraction of these two distance distributions from

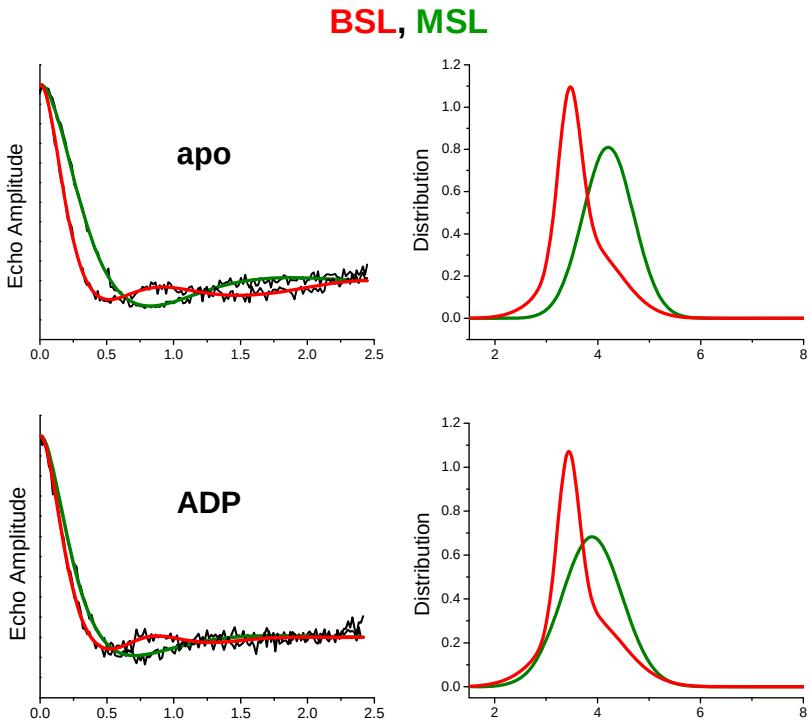

Figure 29 BSL and MSL DEER and distance distributions.
Left: DEER data from BSL at 494.498 and 639.643 (red) and MSL at 498 and 639 (green) on the relay helix. Data was acquired in apo and ADP biochemical states. Right: Distance distributions extracted from DEER data. In both apo and ADP biochemical states the MSL data is bet fit to a one-Gaussian distribution and BSL data is best fit to a two-Gaussian distribution. Distribution parameters are given in **Table 2**.

the BSL waveforms, corresponding to two confirmations of the relay helix, demonstrates the increased resolution provided by the rigid attachment of BSL. The BSL DEER data in this section were acquired by and analyzed by Rebecca J. Moen and Zachary M. James.

Table 2 Distance distributions

Spin label	Biochemical state	R_1 (FWHM), nm	Mole fraction X_1	R_2 (FWHM), nm	Mole fraction X_2
BSL	apo	3.45 (0.73)	0.44	3.78 (2.17)	0.56
	ADP	3.43 (0.70)	0.41	3.75 (2.38)	0.59
MSL	apo	4.10 (1.24)	1	-	-
	ADP	3.97 (1.28)	1	-	-

R, mean distance; FWHM, full width of the Gaussian distribution at half maximum (eq. 4.1); subscripts indicate that DEER data for BSL was best fit to two Gaussian distributions.

4.5 Discussion

Summary of Results

We have used SDSL and EPR to measure the structural dynamics of the relay helix within the CD of *Dictyostelium discoideum* myosin II (S1dC). Conventional EPR was used to measure spin label dynamics and relay helix orientation, and DEER was used to measure the distance distributions between pairs of spin labels (relay helix bending). All measurements were made using two spin labels, BSL and MSL (MSL DEER data was previously published (21)). Conventional EPR of minced fiber bundles decorated with spin-labeled S1dC revealed that the BSL is strongly immobilized on myosin while MSL is weakly immobilized (**Figure 27**). Conventional EPR spectra of oriented fiber bundles

decorated with MSL-S1dC are difficult to analyze to determine an orientational distribution because the effects of nanosecond motions and orientation are difficult to distinguish (both dynamics and orientation affect linewidth and peak position) (**Figure 28**, top). In contrast, BSL is strongly immobilized, meaning spectra can be fit without having to include nanosecond probe motions in the simulation. Oriented BSL spectra reveal two distinct orientational distributions of the relay helix (**Figure 28**, middle). Additionally, BSL reveals that apo and ADP spectra are markedly different, while MSL spectra are essentially identical in apo and ADP biochemical states. Following this trend, DEER waveforms of BSL-S1dC are best fit to a two-Gaussian distance distribution while MSL waveforms reveal only one distance distribution.

Interpretation of Results

The results summarized above have two meaningful interpretations. First, they demonstrate qualitatively that BSL provides greater resolution compared to the monofunctional spin label MSL. The splitting $2T_{\parallel}'$ of the minced BSL spectrum indicates that BSL is strongly immobilized on the protein backbone while the MSL, with substantially smaller $2T_{\parallel}'$, is weakly immobilized (**Figure 27**). This advantage of a strongly immobilized spin label is demonstrated by the orientational measurements and DEER. Oriented spectra of BSL show two well-resolved components that differ in apo and ADP biochemical states, while MSL spectra do not clearly show two components and the apo and ADP spectra are identical (**Figure 28**). Similarly, the BSL DEER waveforms reveal two distance distributions while MSL only reveals one (**Figure 29**).

Collectively, all three measurements, spin label dynamics, relay helix orientation, and distance measurements, clearly demonstrate that BSL provides substantially greater resolution than the monofunctional spin label MSL for measuring protein structural dynamics. An alternative interpretation is that BSL adopts two confirmations on a helix, rather than resolving two structural states of the protein. Though we have not ruled out this possibility (discussed more in 4.6 Future Directions), x-ray crystallography of BSL labeled T4 lysozyme provides strong evidence that the BSL nitroxide adopts one well-ordered confirmation (85).

These results can also be interpreted in the context of myosin structural biology. During the actomyosin ATPase cycle, myosin uses chemical potential energy derived from ATP hydrolysis to generate force on actin during muscle contraction, cell locomotion and intracellular trafficking (21). During force generation myosin undergoes structural transitions that are influenced by ATP binding, hydrolysis and nucleotide release. It has been proposed that the relay helix is a key structure in the coupling of myosin enzymatic activity and motor function (21,86). Using site-directed labeling with monofunctional probes, DEER, and time-resolved fluorescence resonance energy transfer (TR-FRET), previous work in the Thomas Lab has shown that the relay helix can adopt two structural states in ATP and ADP.P_i biochemical states (21). However, DEER and TR-FRET data in apo and ADP states were best fist assuming a one-Gaussian distance distribution. In contrast, the conventional EPR and DEER results from this work reveal two distinct orientations of the relay helix in apo and ADP states (**Figure 28** and **Figure 29**). We interpret this result to show that in apo and ADP biochemical states there is a

partitioning between two structural states of the relay helix, and ADP binding does not cause a bending of the relay helix (as would be indicated in a change in the DEER waveforms between apo and ADP). However, ADP does cause a rotation of the relay helix that is not manifested as a change in the distance distributions. Understanding these nucleotide dependent transitions is essential for a more complete understanding of myosin motor function. Additionally, these methods can be applied to other molecules in which structural dynamics is related to function.

Relationship to other work

At the time of this writing, there are three notable publications in which BSL is used to measure protein structural dynamics. The first work, published in 2008, used BSL to simultaneously crosslink and spin-label myosin, and conventional EPR and STEPR were used to measure the dynamics and orientation of Cys^{707}-Cys^{697} crosslinked myosin on actin (5). EPR spectra revealed that crosslinked myosin was statically disordered on actin, $\tau_R \geq 1$ ms and $\Delta\theta' \geq 90^o$. Using a similar approach, a second study used BSL and STEPR to show that tropomyosin dynamics vary along its length, and troponin decreases tropomyosin dynamics while Ca^{2+} and myosin have no affect (84). A third study labeled T4 lysozyme and intestinal fatty acid-binding protein (iFABP) with BSL (85). Conventional EPR revealed that BSL was strongly immobilized on both proteins (T4 lysozyme and iFABP) at all labeling sites. Distance distributions determined from DEER waveforms demonstrated narrow distributions on both proteins, while the corresponding waveforms from a monofunctional label revealed significantly wider distributions. Also,

an X-ray crystal structure of BSL-labeled T4 lysozyme was solved, indicating a single confirmation of the BSL side chain. The results from all three of these works (5,84,85) are consistent with the findings in this work. Namely, BSL is strongly immobilized on the protein backbone enabling high-resolution measurements of protein dynamics and interprotein distances. Additionally, the work on BSL-labeled T4 lysozyme indicates that BSL preferentially forms two intramolecular disulfide bonds and adopts one energetically relaxed confirmation on an α-helix (85). Considering this result, we have good reason to conclude that the two orientational distributions and distance distributions resolved in the present work represent two structural states of the relay helix, not two confirmations of BSL.

Conclusions

We have used protein mutagenesis, site-directed spin labeling, conventional EPR and DEER to demonstrate that BSL attaches rigidly to an α-helix, and this rigid attachment allows greater resolution when using EPR to measure protein structural dynamics. Conventional EPR of oriented fiber bundles decorated with BSL-S1dC reveals two structural states of the relay helix, and an ADP effect on relay helix orientation. Similarly, DEER waveforms form BSL are best fit to a two-Gaussian distance distribution in apo and ADP biochemical states. Equivalent measurements made using the monofunctional spin label MSL demonstrate probe flexibility and only one orientation of the relay helix. We conclude that BSL spectra and DEER waveforms reveal structural

information that is masked by the nanosecond motions of the monofunctional spin label MSL.

4.6 Future Directions

The project discussed in Chapter 4 is a work in progress. The following items will be carried out in order to complete this project.

Additional labeling sites for measuring helix orientation

The conventional EPR spectra used to determine helix orientation (**Figure 28)** were acquired with BSL at 494.498 and MSL at 498 on the relay helix. Similar measurements will be made on two other helixes within the myosin CD: (i) BSL at 639.643/MSL at 639 and (ii) BSL at 325.329/MSL at 325 (**Figure 30**, left). These additional measurements are needed to demonstrate that the highly ordered spectra from BSL on the relay helix are not

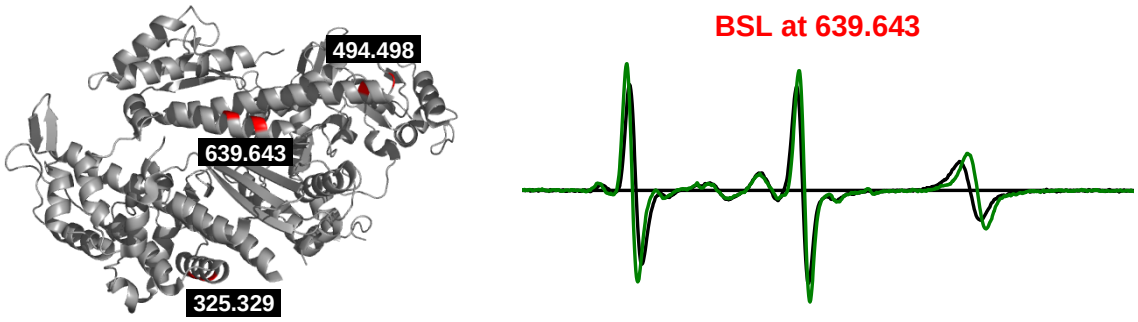

Figure 30 S1dC labeling sites and 639.643 spectra.
Left: S1dC crystal structure (1FMV). Three BSL labeling sites are highlighted in red. Right: Conventional EPR spectra of oriented fiber bundles decorated with spin-labeled S1dC. S1dC was labeled with BSL at 639.643. Spectra were acquired with the fiber bundle oriented parallel to H. Apo spectrum is black and ADP is green.

isolated results (i.e. BSL is strongly immobilized at other labeling sites). Preliminary spectra of BSL at 639.643 reveal orientational distributions similar to the relay helix; spectra with narrow lines indicating a high degree of orientational order and an ADP effect on the orientational distribution (**Figure 30**).

Fitting spectra to determine orientational distributions

As mentioned in Section 4.4, BSL spectra will be analyzed to determine the orientational distribution of the BSL relative to the muscle fiber axis using computational simulation and least-squares minimization (5,26,28). The first step in this analysis is to fit the spectrum of minced fiber bundle (**Figure 27**) to obtain the orientation-independent parameters, including the anisotropic T and g tensors and the linewidths. Spectra of oriented fiber bundles will then be fit to determine the orientational distribution of the spin label relative to the fiber axis, defined by the center (θ_0') and the width ($\Delta\theta'$, full width at half-maximum) of the assumed Gaussian orientational distributions (see Section 2.8 for more detail on fitting EPR spectra). The resolution of this analysis is greatly enhanced by the use of BSL over a monofunctional spin label. Given that BSL is strongly immobilized on a helix (**Figure 27**), it is possible to fit the oriented BSL spectra without having to include nanosecond probe motions in the simulation, which greatly simplifies the simulation. Additionally, the rigid coupling between BSL and the helix backbone indicates that the orientational distributions determined from the fits are not polluted by the flexibility of the spin label. Rather, the orientational distributions accurately describe the structure of the protein!

Quantitate the extent of labeling

Whenever a protein is labeled with a site-specific probe, it is important to quantitate the extent of labeling (labels per protein), as was demonstrated in Chapter 3 for the RLC spin-labeled with FDNASL (Section 3.6). We will use the same approaches described in Chapter 3 to measure the extent of BSL and MSL labeling of S1dC. That is, the number of spin labels per S1dC will be determined by digital analysis of EPR spectra (71) and by electrospray mass spectrometry (70). Digital analysis of the EPR spectrum from S1dC labeled at 494.498 with BSL indicates 1.16 BSL per myosin, indicating there may be a small amount of nonspecific or monofunctionally attached BSL. If this result is consistent and confirmed with mass spectrometry, we will modify the labeling protocol to reduce over labeling.

Measuring S1dC ATPase activity

An important control in this work is to verify that spin-labeling does not significantly perturb the enzymatic function of S1dC. This will be done by measuring the dependence of myosin ATPase on actin concentration as described previously (21). We do not expect spin-labeling to dramatically alter myosin ATPase. Previous measurements from S1dC, labeled with the monofunctional equivalents of the BSL constructs used in this work, show that labeling had only a minor effect on myosin ATPase (21).

Bibliography

1. Bagshaw, C. R. 1993. Muscle Contraction. New York: Chapman & Hall. 155 p.

2. Labeit, S. and B. Kolmerer. 1995. Titins: giant proteins in charge of muscle ultrastructure and elasticity. Science 270:293-296.

3. Ackermann, M. A. and A. Kontrogianni-Konstantopoulos. Myosin binding protein-C: a regulator of actomyosin interaction in striated muscle. J Biomed Biotechnol 2011:636403.

4. Witt, C. C., C. Burkart, D. Labeit, M. McNabb, Y. Wu, H. Granzier, and S. Labeit. 2006. Nebulin regulates thin filament length, contractility, and Z-disk structure in vivo. Embo J 25:3843-3855.

5. Thompson, A. R., N. Naber, C. Wilson, R. Cooke, and D. D. Thomas. 2008. Structural dynamics of the actomyosin complex probed by a bifunctional spin label that cross-links SH1 and SH2. Biophys J 95:5238-5246.

6. Thomas, D., S. Ramachandran, O. Roopnarine, D. Hayden, and E. Ostap. 1995. The mechanism of force generation in myosin: a disorder-to-order transition, coupled to internal structural changes. Biophysical journal 68:135S-141S.

7. Thomas, D. D., D. Kast, and V. L. Korman. 2009. Site-directed spectroscopic probes of actomyosin structural dynamics. Annu Rev Biophys 38:347-369.

8. Taylor, K., H. Schmitz, M. Reedy, Y. Goldman, C. Franzini-Armstrong, H. Sasaki, R. Tregear, K. Poole, C. Lucaveche, R. Edwards, L. Chen, H. Winkler, and M. Reedy. 1999. Tomographic 3D reconstruction of quick-frozen, Ca2+-activated contracting insect flight muscle. Cell 99:421-431.

9. LaConte, L. E., J. E. Baker, and D. D. Thomas. 2003. Transient kinetics and mechanics of myosin's force-generating rotation in muscle: resolution of millisecond rotational transitions in the spin-labeled myosin light-chain domain. Biochemistry 42:9797-9803.

10. Rayment, I., W. R. Rypniewski, K. Schmidt-Base, R. Smith, D. R. Tomchick, M. M. Benning, D. A. Winkelmann, G. Wesenberg, and H. M. Holden. 1993. Three-dimensional structure of myosin subfragment-1: a molecular motor. Science 261:50-58.

11. Berger, C. L. and D. D. Thomas. 1994. Rotational dynamics of actin-bound intermediates of the myosin adenosine triphosphatase cycle in myofibrils. Biophys J 67:250-261.

12. Thomas, D. D., D. Kast, and V. L. Korman. 2009. Site-Directed Spectroscopic Probes of Actomyosin Structural Dynamics. Annu. Rev. Biophys. 38:347-369.

13. Dominguez, R., Y. Freyzon, K. M. Trybus, and C. Cohen. 1998. Crystal structure of a vertebrate smooth muscle myosin motor domain and its complex with the essential light chain: visualization of the pre- power stroke state. Cell 94:559-571.

14. Rayment, I., H. M. Holden, M. Whittaker, C. B. Yohn, M. Lorenz, K. C. Holmes, and R. A. Milligan. 1993. Structure of the actin-myosin complex and its implications for muscle contraction. Science 261:58-65.

15. Takagi, Y., H. Shuman, and Y. E. Goldman. 2004. Coupling between phosphate release and force generation in muscle actomyosin. Philos Trans R Soc Lond B Biol Sci 359:1913-1920.

16. Smith, D. A. and J. Sleep. 2004. Mechanokinetics of rapid tension recovery in muscle: the Myosin working stroke is followed by a slower release of phosphate. Biophys J 87:442-456.

17. White, H. D., B. Belknap, and M. R. Webb. 1997. Kinetics of Nucleoside Triphosphate Cleavage and Phosphate Release Steps by Associated Rabbit Skeletal Actomyosin, Measured Using a Novel Fluorescent Probe for Phosphate. Biochemistry 36:11828-11836.

18. Campbell, I. D. and R. A. Dwek. 1984. Biological Spectroscopy: Benjamin-Cummings.

19. Griffiths, D. J. 2005. Introduction to Quantum Mechanics: Pearson Prentice Hall.

20. Baker, J. E., I. Brust-Mascher, S. Ramachandran, L. E. LaConte, and D. D. Thomas. 1998. A large and distinct rotation of the myosin light chain domain occurs upon muscle contraction. Proc Natl Acad Sci U S A. p 2944-2949.

21. Agafonov, R. V., I. V. Negrashov, Y. V. Tkachev, S. E. Blakely, M. A. Titus, D. D. Thomas, and Y. E. Nesmelov. 2009. Structural dynamics of the myosin relay helix by time-resolved EPR and FRET. Proc Natl Acad Sci U S A.

22. LaConte, L. E., V. Voelz, W. Nelson, M. Enz, and D. D. Thomas. 2002. Molecular dynamics simulation of site-directed spin labeling: experimental validation in muscle fibers. Biophys J 83:1854-1866.

23. Squier, T. C. and D. D. Thomas. 1986. Methodology for increased precision in saturation transfer electron paramagnetic resonance studies of rotational dynamics. Biophys J 49:921-935.

24. Thomas, D. D. 1977. Saturation transfer EPR. Trends Biochem Sci 2:N62-N63.

25. Fajer, P. G. 2000. Electron Spin Resonance Spectroscopy Labeling in Peptide and Protein Analysis. In Encyclopedia of Analytical Chemistry. R. A. Meyers, editor. John Wiley & Sons Ltd. Chidester. 5725-5761.

26. Fajer, P. G., R. L. H. Bennett, C. F. Polnaszek, E. A. Fajer, and D. D. Thomas. 1990. General method for multiparameter fitting of high-resolution EPR spectra using a simplex algorithm. J. Magn. Res. 88:111-125.

27. Barnett, V. A., P. G. Fajer, C. F. Polnaszek, and D. D. Thomas. 1986. High-resolution detection of muscle crossbridge orientation by electron paramagnetic resonance. Biophys J 49:144-147.

28. Thomas, D. D. and R. Cooke. 1980. Orientation of spin-labeled myosin heads in glycerinated muscle fibers. Biophys J 32:891-906.

29. Cooke, R., M. S. Crowder, and D. D. Thomas. 1982. Orientation of spin labels attached to cross-bridges in contracting muscle fibres. Nature 300:776-778.

30. Hambly, B., K. Franks, and R. Cooke. 1991. Orientation of spin-labeled light chain-2 exchanged onto myosin cross-bridges in glycerinated muscle fibers. Biophys J 59:127-138.

31. Berger, C. L., E. C. Svensson, and D. D. Thomas. 1989. Photolysis of a photolabile precursor of ATP (caged ATP) induces microsecond rotational motions of myosin heads bound to actin. Proc Natl Acad Sci U S A 86:8753-8757.

32. Berger, C. L. and D. D. Thomas. 1993. Rotational dynamics of actin-bound myosin heads in active myofibrils. Biochemistry 32:3812-3821.

33. Berger, C. L. and D. D. Thomas. 1991. Rotational dynamics of actin-bound intermediates in the myosin ATPase cycle. Biochemistry 30:11036-11045.

34. Craig, R., L. E. Greene, and E. Eisenberg. 1985. Structure of the actin-myosin complex in the presence of ATP. Proc Natl Acad Sci U S A 82:3247-3251.

35. Walker, M., J. Trinick, and H. White. 1995. Millisecond time resolution electron cryo-microscopy of the M-ATP transient kinetic state of the acto-myosin ATPase. Biophys J 68:87S-91S.

36. Walker, M., H. White, B. Belknap, and J. Trinick. 1994. Electron cryomicroscopy of acto-myosin-S1 during steady-state ATP hydrolysis. Biophys J 66:1563-1572.

37. Prochniewicz, E., T. F. Walseth, and D. D. Thomas. 2004. Structural dynamics of actin during active interaction with myosin: different effects of weakly and strongly bound myosin heads. Biochemistry 43:10642-10652.

38. Werber, M. M., Y. M. Peyser, and A. Muhlrad. 1992. Characterization of stable beryllium fluoride, aluminum fluoride, and vanadate containing myosin subfragment 1-nucleotide complexes. Biochemistry 31:7190-7197.

39. Pate, E. and R. Cooke. 1988. Energetics of the actomyosin bond in the filament array of muscle fibers. Biophys J 53:561-573.

40. Fajer, P. G., E. A. Fajer, N. J. Brunsvold, and D. D. Thomas. 1988. Effects of AMPPNP on the orientation and rotational dynamics of spin-labeled muscle cross-bridges. Biophys J 53:513-524.

41. Takacs, B., N. Billington, M. Gyimesi, B. Kintses, A. Malnasi-Csizmadia, P. J. Knight, and M. Kovacs. Myosin complexed with ADP and blebbistatin reversibly adopts a conformation resembling the start point of the working stroke. Proc Natl Acad Sci U S A 107:6799-6804.

42. Greene, L., J. Chalovich, and E. Eisenberg. 1986. Effect of nucleotide on the binding of N,N'-p-phenylenedimaleimide-modified S-1 to unregulated and regulated actin. Biochemistry 25:704-709.

43. Chalovich, J., L. Greene, and E. Eisenberg. 1983. Crosslinked myosin subfragment 1: a stable analogue of the subfragment-1.ATP complex. Proc Natl Acad Sci USA 80:4909-4913.

44. Bobkov, A. and E. Reisler. 2000. Is SH1-SH2-cross-linked myosin subfragment 1 a structural analog of the weakly-bound state of myosin? Biophysical journal 79:460-467.

45. Chaen, S., M. Shimada, and H. Sugi. 1986. Evidence for cooperative interactions of myosin heads with thin filament in the force generation of vertebrate skeletal muscle fibers. J Biol Chem 261:13632-13636.

46. Barnett, V. A., A. Ehrlich, and M. Schoenberg. 1992. Formation of ATP-insensitive weakly-binding crossbridges in single rabbit psoas fibers by treatment with phenylmaleimide or para-phenylenedimaleimide. Biophys J 61:358-367.

47. Prochniewicz, E., D. A. Lowe, D. J. Spakowicz, L. Higgins, K. O'Conor, L. V. Thompson, D. A. Ferrington, and D. D. Thomas. 2008. Functional, structural, and chemical changes in myosin associated with hydrogen peroxide treatment of skeletal muscle fibers. Am J Physiol Cell Physiol 294:C613-626.

48. Roopnarine, O. and D. D. Thomas. 1995. Orientational dynamics of indane dione spin-labeled myosin heads in relaxed and contracting skeletal muscle fibers. Biophys J 68:1461-1471.

49. Hambly, B., K. Franks, and R. Cooke. 1992. Paramagnetic probes attached to a light chain on the myosin head are highly disordered in active muscle fibers. Biophys J 63:1306-1313.

50. Barnett, V. A. and D. D. Thomas. 1989. Microsecond rotational motion of spin-labeled myosin heads during isometric muscle contraction. Saturation transfer electron paramagnetic resonance. Biophys J 56:517-523.

51. Roopnarine, O., A. G. Szent-Gyorgyi, and D. D. Thomas. 1998. Microsecond rotational dynamics of spin-labeled myosin regulatory light chain induced by relaxation and contraction of scallop muscle. Biochemistry 37:14428-14436.

52. Ramachandran, S. and D. D. Thomas. 1999. Rotational dynamics of the regulatory light chain in scallop muscle detected by time-resolved phosphorescence anisotropy. Biochemistry 38:9097-9104.

53. Thomas, D. D., L. R. Dalton, and J. S. Hyde. 1976. Rotational diffusion studied by passage saturation transfer electron paramagnetic resonance. J Chem Phys 65.

54. Roopnarine, O. 2003. Mechanical defects of muscle fibers with myosin light chain mutants that cause cardiomyopathy. Biophys J 84:2440-2449.

55. Corrie, J. E., B. D. Brandmeier, R. E. Ferguson, D. R. Trentham, J. Kendrick-Jones, S. C. Hopkins, U. A. van der Heide, Y. E. Goldman, C. Sabido-David, R. E. Dale, S. Criddle, and M. Irving. 1999. Dynamic measurement of myosin light-chain-domain tilt and twist in muscle contraction. Nature 400:425-430.

56. Burghardt, T. P., J. Li, and K. Ajtai. 2009. Single myosin lever arm orientation in a muscle fiber detected with photoactivatable GFP. Biochemistry 48:754-765.

57. Ostap, E. M., V. A. Barnett, and D. D. Thomas. 1995. Resolution of three structural states of spin-labeled myosin in contracting muscle. Biophys J 69:177-188.

58. Himmel, D. M., S. Gourinath, L. Reshetnikova, Y. Shen, A. G. Szent-Gyorgyi, and C. Cohen. 2002. Crystallographic findings on the internally uncoupled and near-rigor states of myosin: further insights into the mechanics of the motor. Proc Natl Acad Sci U S A 99:12645-12650.

59. Houdusse, A., V. Kalabokis, D. Himmel, A. Szent-Gyorgyi, and C. Cohen. 1999. Atomic structure of scallop myosin subfragment S1 complexed with MgADP: a novel conformation of the myosin head. Cell 97:459-470.

60. Houdusse, A., A. G. Szent-Gyorgyi, and C. Cohen. 2000. Three conformational states of scallop myosin S1. Proc Natl Acad Sci U S A 97:11238-11243.

61. Huston, E. E., J. C. Grammer, and R. G. Yount. 1988. Flexibility of the myosin heavy chain: direct evidence that the region containing SH1 and SH2 can move 10 A under the influence of nucleotide binding. Biochemistry 27:8945-8952.

62. Nitao, L. K. and E. Reisler. 1998. Probing the conformational states of the SH1-SH2 helix in myosin: a cross-linking approach. Biochemistry 37:16704-16710.

63. Barnett, V. A. and D. D. Thomas. 1987. Resolution of conformational states of spin-labeled myosin during steady-state ATP hydrolysis. Biochemistry 26:314-323.

64. Agafonov, R. V., Y. E. Nesmelov, M. A. Titus, and D. D. Thomas. 2008. Muscle and nonmuscle myosins probed by a spin label at equivalent sites in the force-generating domain. Proc Natl Acad Sci U S A 105:13397-13402.

65. Gourinath, S., D. M. Himmel, J. H. Brown, L. Reshetnikova, A. G. Szent-Gyorgyi, and C. Cohen. 2003. Crystal structure of scallop Myosin s1 in the pre-power stroke state to 2.6 a resolution: flexibility and function in the head. Structure (Camb) 11:1621-1627.

66. Allingham, J. S., R. Smith, and I. Rayment. 2005. The structural basis of blebbistatin inhibition and specificity for myosin II. Nat Struct Mol Biol 12:378-379.

67. Nesmelov, Y. E., R. V. Agafonov, I. V. Negrashov, S. E. Blakely, M. A. Titus, and D. D. Thomas. 2011. Structural kinetics of myosin by transient time-resolved FRET. Proc Natl Acad Sci U S A 108:1891-1896.

68. Ling, N., C. Shrimpton, J. Sleep, J. Kendrick-Jones, and M. Irving. 1996. Fluorescent probes of the orientation of myosin regulatory light chains in relaxed, rigor, and contracting muscle. Biophys J 70:1836-1846.

69. Nelson, W. D., S. E. Blakely, Y. E. Nesmelov, and D. D. Thomas. 2005. Site-directed spin labeling reveals a conformational switch in the phosphorylation domain of smooth muscle myosin. Proc Natl Acad Sci U S A 102:4000-4005.

70. Kast, D., L. M. Espinoza-Fonseca, C. Yi, and D. D. Thomas. 2010. Phosphorylation-induced structural changes in smooth muscle myosin regulatory light chain. Proc Natl Acad Sci U S A 107:8207-8212.

71. Karim, C. B., Z. Zhang, and D. D. Thomas. 2007. Synthesis of TOAC spin-labeled proteins and reconstitution in lipid membranes. Nat Protoc 2:42-49.

72. Burghardt, T. P., K. Ajtai, D. K. Chan, M. F. Halstead, J. Li, and Y. Zheng. 2007. GFP-tagged regulatory light chain monitors single myosin lever-arm orientation in a muscle fiber. Biophys J 93:2226-2239.

73. Moss, R. L., G. G. Giulian, and M. L. Greaser. 1982. Physiological effects accompanying the removal of myosin LC2 from skinned skeletal muscle fibers. J Biol Chem 257:8588-8591.

74. Madden, T. D., D. Chapman, and P. J. Quinn. 1979. Cholesterol modulates activity of calcium-dependent ATPase of the sarcoplasmic reticulum. Nature 279:538-541.

75. Karim, C. B., M. G. Paterlini, L. G. Reddy, G. W. Hunter, G. Barany, and D. D. Thomas. 2001. Role of cysteine residues in structural stability and function of a transmembrane helix bundle. J Biol Chem 276:38814-38819.

76. Fabiato, A. and F. Fabiato. 1979. Calculator programs for computing the composition of the solutions containing multiple metals and ligands used for experiments in skinned muscle cells. J Physiol (Paris) 75:463-505.

77. Lanzetta, P. A., L. J. Alvarez, P. S. Reinach, and O. A. Candia. 1979. An improved assay for nanomole amounts of inorganic phosphate. Anal Biochem 100:95-97.

78. Kovacs, M., J. Toth, C. Hetenyi, A. Malnasi-Csizmadia, and J. R. Sellers. 2004. Mechanism of blebbistatin inhibition of myosin II. J Biol Chem 279:35557-35563.

79. Hubbell, W. L., D. S. Cafiso, and C. Altenbach. 2000. Identifying conformational changes with site-directed spin labeling. Nat Struct Biol 7:735-739.

80. Nesmelov, Y. E., R. V. Agafonov, A. Burr, R. T. Weber, and D. D. Thomas. 2008. Structure and dynamics of the force generating domain of myosin probed by site-directed spin labeling and multifrequency electron paramagnetic resonance. Biophys J in press.

81. Lowe, D. A., J. T. Surek, D. D. Thomas, and L. V. Thompson. 2001. Electron paramagnetic resonance reveals age-related myosin structural changes in rat skeletal muscle fibers. Am J Physiol Cell Physiol 280:C540-547.

82. Barnett, V. A. and D. D. Thomas. 1984. Saturation transfer electron paramagnetic resonance of spin-labeled muscle fibers. Dependence of myosin head rotational motion on sarcomere length. J Mol Biol 179:83-102.

83. Columbus, L. and W. L. Hubbell. 2004. Mapping backbone dynamics in solution with site-directed spin labeling: GCN4-58 bZip free and bound to DNA. Biochemistry 43:7273-7287.

84. Rayes, R. F., T. Kalai, K. Hideg, M. A. Geeves, and P. G. Fajer. 2011. Dynamics of tropomyosin in muscle fibers as monitored by saturation transfer EPR of bi-functional probe. PLoS One 6:e21277.

85. Fleissner, M. R., M. D. Bridges, E. K. Brooks, D. Cascio, T. Kalai, K. Hideg, and W. L. Hubbell. Structure and dynamics of a conformationally constrained nitroxide side chain and applications in EPR spectroscopy. Proc Natl Acad Sci U S A 108:16241-16246.

86. Tsiavaliaris, G., S. Fujita-Becker, R. Batra, D. I. Levitsky, F. J. Kull, M. A. Geeves, and D. J. Manstein. 2002. Mutations in the relay loop region result in dominant-negative inhibition of myosin II function in Dictyostelium. EMBO Rep 3:1099-1105.

87. Korman, V. L., S. E. Anderson, E. Prochniewicz, M. A. Titus, and D. D. Thomas. 2006. Structural dynamics of the actin-myosin interface by site-directed spectroscopy. J Mol Biol 356:1107-1117.

88. Shih, W. M., Z. Gryczynski, J. R. Lakowicz, and J. A. Spudich. 2000. A FRET-based sensor reveals large ATP hydrolysis-induced conformational changes and three distinct states of the molecular motor myosin. Cell 102:683-694.

89. Pannier, M., S. Veit, A. Godt, G. Jeschke, and H. W. Spiess. 2000. Dead-time free measurement of dipole-dipole interactions between electron spins. J Magn Reson 142:331-340.

90. Jeschke, G., V. Chechik, P. Ionita, A. Godt, H. Zimmermann, J. Banham, C. R. Timmel, D. Hilger, and H. Jung. 2006. Appl. Magn. Reson. 30:473-498.

91. Milov, A. D., A. B. Ponomarev, and Y. D. Tsvetkov. 1984. Electron-Electron Double Resonance in Electron Spin Echo: Model Biradical Systems and the Sensitized Photolysis of Decalin. Chem. Phys. Lett. 110:67-72.

92. Klein, J. C., A. R. Burr, B. Svensson, D. J. Kennedy, J. Allingham, M. A. Titus, I. Rayment, and D. D. Thomas. 2008. Actin-binding cleft closure in myosin II probed by site-directed spin labeling and pulsed EPR. Proc Natl Acad Sci U S A 105:12867-12872.